

Modeling of dynamic cerebrovascular reactivity to spontaneous and externally induced CO₂ fluctuations in the human brain using BOLD-fMRI

Prokopis C. Prokopiou^a, Kyle T.S. Pattinson^b, Richard G. Wise^c, Georgios D. Mitsis^{d,a,*}

^a*Integrated Program in Neuroscience, McGill University, Montreal Neurological Institute, H3A 2B4, QC, Canada*

^b*Nuffield Department of Anaesthetics, University of Oxford, John Radcliffe Hospital, Oxford OX3 9DU, UK*

^c*CUBRIC, School of Psychology, University of Cardiff, CF10 3AT, UK*

^d*Department of Bioengineering, McGill University, Montreal, QC, H3A 0C3, Canada*

Abstract

In this work, we investigate the regional characteristics of the dynamic interactions between arterial CO₂ and BOLD (dynamic cerebrovascular reactivity - dCVR) during normal breathing and hypercapnic, externally induced step CO₂ challenges. To obtain dCVR curves at each voxel, we use a custom set of basis functions based on the Laguerre and gamma basis sets. This allows us to obtain robust dCVR estimates both in larger regions of interest (ROIs), as well as in individual voxels. We also implement classification schemes to identify brain regions with similar dCVR characteristics. Our results reveal considerable variability of dCVR across different brain regions, as well as during different experimental conditions (normal breathing and hypercapnic challenges), suggesting a differential response of cerebral vasculature to spontaneous CO₂ fluctuations and larger, externally induced CO₂ changes that are possibly associated with the underlying differences in mean arterial CO₂ levels. The clustering results suggest that anatomically distinct brain regions are characterized by different dCVR curves that in some cases do not exhibit the standard, positive valued curves that have been previously reported. They also reveal a consistent set of dCVR cluster shapes for resting and forcing conditions, which exhibit different distribution patterns across brain voxels.

Keywords: Dynamic cerebrovascular reactivity, BOLD; carbon dioxide; fMRI; dynamic end-tidal forcing; hypercapnia; normal breathing

1. Introduction

Cerebral blood flow (CBF) is regulated by multifactorial homeostatic mechanisms that maintain its value relatively constant. The ability of the brain to achieve this in response to changes in perfusion pressure is termed cerebral autoregulation (Lucas et al., 2010; Mitsis et al., 2004, 2002; Panerai, 1998; Tzeng and Ainslie, 2014). In addition to perfusion pressure, the cerebrovascular bed is highly responsive to local tissue metabolism (Attwell et al., 2010; Iadecola and Nedergaard, 2007) and arterial levels of carbon dioxide (CO₂) (Battisti-Charbonney et al., 2011; Brugniaux et al., 2007; Duffin, 2011; Ratnatunga and Adiseshiah, 1990). The CBF response to arterial CO₂ changes

* Corresponding author. Tel.: +1-514-398-4344.
E-mail address: georgios.mitsis@mcgill.ca

is termed cerebrovascular reactivity (CVR[†]) and can be assessed, among other experimental modalities, using functional magnetic resonance imaging (fMRI) (Tancredi and Hoge, 2013; Wise et al., 2004; Yezhuvath et al., 2009). Also, the important role of CVR in cerebral autoregulation has been suggested (Mitsis et al., 2004; Tzeng et al., 2014).

To assess CVR, resting fluctuations in arterial CO₂ (Golestani et al., 2015; Mitsis et al., 2004; Prokopiou et al., 2016; Wise et al., 2004), arterial gas manipulation protocols such as end-tidal forcing and prospective control (Blockley et al., 2011; Pattinson et al., 2009; Slessarev et al., 2007; Wise et al., 2007) or, more recently, sinusoidally modulated gas stimuli (Blockley et al., 2017) and controlled breathing (Bright and Murphy, 2013; Murphy et al., 2011) have been used. The advantages of CO₂ as a vasoactive stimulus have been suggested (Fierstra et al., 2013). Also, resting fluctuations are a desirable stimulus as they remove the need for any external interventions, making it applicable to all populations.

When PaCO₂ changes with respect to normocapnia, assuming that oxygen consumption remains constant, the blood-oxygen-level-dependent signal obtained with functional magnetic resonance imaging (BOLD-fMRI) can be used as a surrogate for changes in regional CBF (Fierstra et al., 2013). This enables the acquisition of time series with a high spatial resolution, which reflect the sensitivity of the cerebrovascular bed to contemporaneous changes in PaCO₂, and allow for investigation of the variability of CVR in different regions of the brain. The vast majority of BOLD-based CVR studies define and quantify CVR as the percent change in the BOLD signal per unit increase in CO₂ (Fierstra et al., 2013). While the largest portion of the literature deals with regions of interest (ROIs) defined in the gray matter (GM) where the signal-to-noise ratio (SNR) is high (Bokkers et al., 2010; Bright and Murphy, 2013; Wise et al., 2004; Yezhuvath et al., 2009), a few studies have investigated CVR in the brain white matter (WM) (Bhogal et al., 2015; Thomas et al., 2014) and ventricles (Thomas et al., 2013). Although the SNR in these structures is considerably lower, which makes measuring CVR with BOLD challenging, the aforementioned studies have provided evidence that CVR in the brain WM is positive but significantly lower than in the GM, and that cerebrospinal fluid (CSF)-rich regions in the brain, such as the lateral ventricles, exhibit a negative BOLD-CVR. These negative BOLD responses to PaCO₂ challenges were attributed to partial volume effects and to dilation of ventricular vessels accompanied by shrinkage in CSF space (Thomas et al., 2013).

Recent studies have also investigated the dynamic interactions between hypercapnic, externally induced step CO₂ challenges and the BOLD signal, i.e. dynamic CVR (dCVR) (Duffin et al., 2015; Poublanc et al., 2015). Dynamic CVR quantifies the transient changes in CBF that occur in response to abrupt changes in PaCO₂ and it is an intrinsic property of the cerebral vasculature related to elastance and compliance. It determines how fast or slow CBF reaches its steady-state value. On the other hand, steady-state CVR refers to the equilibrium condition that occurs as the effects of transients are no longer important and ignores the time-course of the transient response. In (Duffin et al., 2015; Poublanc et al., 2015), the response delay observed between CO₂ and BOLD was associated to the time constant of a linear monoexponential curve. This time constant was estimated in a voxel-wise manner for a group of patients with diagnosed steno-occlusive disease. The estimated response delay at each voxel was then used to identify regions with reduced vasodilatory reserve, associated with the disease pathophysiology. Along these lines, (Donahue et al., 2016) also showed significant differences in CVR response delays between a group of healthy subjects and a group of subjects with intracranial stenosis using simple respiratory challenges and cross correlation techniques.

The main purpose of the present study is to investigate in detail the regional characteristics of dCVR in the human brain using spontaneous (resting-state) and hypercapnic step changes in CO₂ (end-tidal forcing), and BOLD-fMRI. We initially conduct our analysis in larger, functionally defined ROIs that are possibly involved in the brainstem

[†] Although CVR is strictly defined as the CBF response to any vasoactive or vasoconstrictive stimulus, it is more frequently employed in the literature to denote the CBF response to arterial CO₂ changes. For consistency with this literature, this notation is adopted in this work as well.

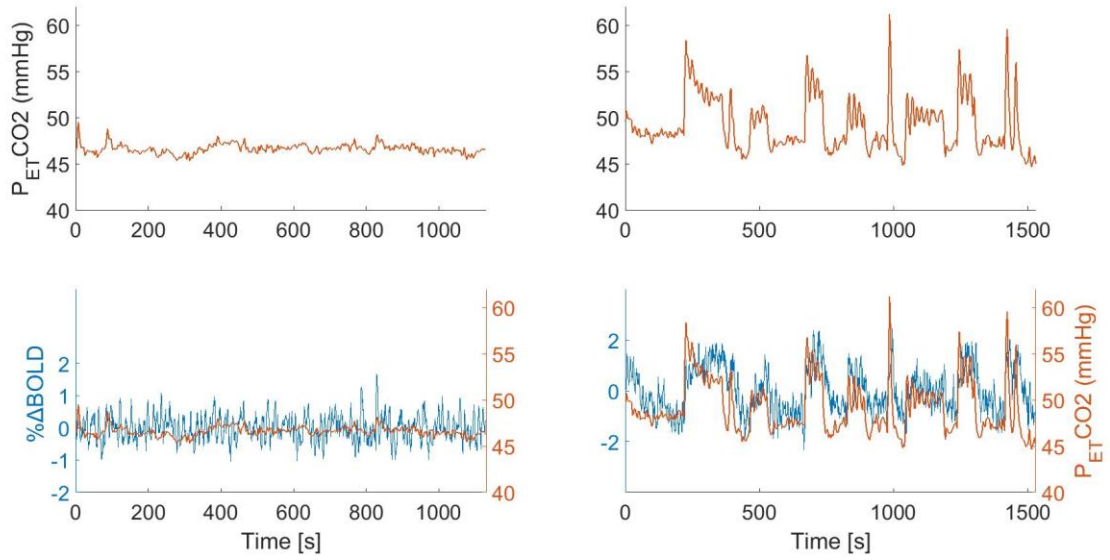


Fig. 1. Example of changes in $P_{ET}CO_2$ and BOLD in one representative subject. Left panels: resting breathing, Right panels: CO_2 challenges. The bottom panels show the $P_{ET}CO_2$ traces along the corresponding (unshifted) BOLD traces.

respiratory control network of the human brain (Pattinson et al., 2009), as well as in structurally defined ROIs. To this end, we use both linear and nonlinear models based on Laguerre function expansions and we show that the effects of CO_2 on the BOLD signal are predominantly linear for both experimental conditions. Subsequently, we investigate the regional variability of dCVR over the entire scan field of view in a voxel-wise fashion. To achieve this, we construct a custom basis set based on Laguerre and gamma functions to achieve robust estimation using functional expansions that reduce the number of required free parameters (Marmarelis, 2004), and we estimate voxel-specific dCVR curves. We subsequently use the results to construct maps of key dCVR curve features such as total area, peak value, time-to-peak, and power, for each experimental condition, and we use the dCVR feature maps to perform statistical comparisons between the two experimental conditions. Finally, we perform clustering analysis on the estimated voxel-specific dCVR curves to identify brain regions with similar dCVR characteristics. Our results suggest that it is possible to obtain reliable dCVR estimates from spontaneous fluctuations using the proposed methodology. The spontaneous and forcing dCVR curves overall exhibit similar characteristics; however, regionally specific differences that are protocol-specific are also revealed. Finally, the clustering analysis suggests the existence of several different dCVR shapes with considerably different characteristics that are correlated to different major brain anatomical structures.

2. Methods

2.1. Experimental methods

This work is an extended analysis of the experimental data presented in (Pattinson et al., 2009). 12 right-handed healthy volunteers aged 32 ± 5 years (3 female) participated in this study after giving written informed consent in accordance with the Oxfordshire Clinical Research Ethics committee.

2.1.1. Respiratory protocol

During scanning sessions, subjects were fitted with a facemask (Hans Rudolph, Kansas City, MO, USA) attached

to a breathing system, which delivered mixtures of air, O₂, and CO₂. Continuous recordings of tidal CO₂ and O₂ (CD-3A and S-3A; AEI Technologies, Pittsburgh, PA, USA), respiratory volume (VMM-400, Interface Associates, Laguna Niguel, CA, USA) and oxygen saturations (9500 Multigas Monitor, MR Equipment Corp., NY, USA), were acquired. It has been suggested that the end-tidal partial pressure of CO₂ (P_{ET}CO₂) is a suitable surrogate for PaCO₂, and therefore, P_{ET}CO₂ can be used as the stimulus for CBF (Hoskins, 1990; Mark et al., 2011; Robbins et al., 1990; Wise et al., 2004).

The study was divided into two parts. The first part of the study was a resting-state experiment. In the second part of the study, P_{ET}CO₂ and P_{ET}O₂ were targeted using dynamic end-tidal forcing (DEF) (Robbins et al., 1982). The CO₂ challenges were delivered via a computer controlled gas mixing system (Wise et al., 2007). The CO₂ challenges were designed to raise the subjects' P_{ET}CO₂ by either 2 or 4 mmHg above a baseline level maintained at 1 mmHg above their natural P_{ET}CO₂. Representative P_{ET}CO₂ time series during both conditions are shown in Fig. 1.

2.1.2. BOLD imaging

Two thousand seven hundred T2* weighted echo planar imaging (EPI) volumes were acquired on a Siemens Trio 3T scanner. Sequence parameters: TR/TE = 1000/30 ms (Repetition/Echo Time), Voxel size = 2.5 × 2.5 × 2.5 mm, 16 slices, Slice thickness = 3 mm, Field of View (FOV) = 160 × 160 mm, Flip Angle (FA) = 70°, Acquisition matrix = 64 × 64 (RO × PE), Bandwidth = 1954 Hz/Px.

The scan field of view was chosen in the original study (Pattinson et al., 2009) aiming to enhance imaging of the brainstem and the noninvasive imaging of human respiratory centers. It comprised 16 oblique coronal slices of the brainstem. The coronal-oblique sequence parameters used were selected based on pilot studies as they yielded less distortion compared to axial acquisitions and reliable images of the whole brainstem extending rostrally to the putamen, and thalamus. The cortical area above the corpus collosum was excluded from the scanning field for two reasons: (i) there was an inconsistent overlap in cortical areas between subjects, therefore, the remaining area was small, and (ii) there was some image contamination (MRI wrapping) from the brainstem.

Although the study was divided in two parts, scanning was continuous. The first 1130 images (18 minutes, 50 seconds) comprised the normal breathing (resting state) experiment. The duration of the first part of the study was determined based upon (Wise et al., 2004), but was prolonged to account for the lower SNR in the brainstem. The final 1530 images (25 minutes, 30 seconds) comprised the CO₂ stimulation experiment. The duration of the second part was determined by adaptation of a similar CO₂ challenge protocol (Pedersen et al., 1999) for use in the MRI scanner. A high resolution T1-weighted structural scan (voxel size 1 × 1 × 1 mm³) was also acquired to aid registration to a common stereotactic space of reference.

Despite the fact that the BOLD images were collected in a limited field of view, the examined dataset is particularly suitable for modelling the dynamic effects of CVR on the BOLD fMRI signal, as image acquisition was rapid (TR=1s) and a large number of volumes was acquired. Importantly, the dataset includes implementation of a carefully designed forcing protocol that consists of a multi-frequency binary sequence for P_{ET}CO₂ that was specifically devised to spread its power in the frequency domain for maximally stimulating both the central and peripheral chemoreceptor (Pedersen et al., 1999). This makes it ideal for the analyses performed here – including comparison of the obtained dCVR curves between forcing and resting data, as the P_{ET}CO₂ spectrum exhibited a similar form during both conditions.

2.2. Data analysis

2.2.1. Data preprocessing

The basic pre-statistical analysis of the data was carried out using FSL (FMRIB, Oxford, UK (Jenkinson et al.,

2012)), as has been previously described in (Pattinson et al., 2009). In brief, pre-processing of the BOLD images included spatial smoothing by using a Gaussian kernel of 3.5 mm FWHM, high-pass temporal filtering, motion realignment, registration with T1-weighted anatomic images, and normalization to the Montreal Neurological Institute (MNI)-152 template space, with resolution of $2 \times 2 \times 2 \text{ mm}^3$. Furthermore, functional ROIs were obtained in the MNI space, corresponding to areas that revealed increased activity in response to the hypercapnic CO₂ challenges (rostral dorsal pons (Kölliker-Fuse / parabrachial nucleus), left ventral posterior lateral nucleus of the thalamus, left ventrolateral and left ventroanterior nuclei of the thalamus). Also, structural ROIs were defined in areas that were not found to be significantly activated in response to CO₂ challenges (cerebellum, cingulate gyrus, temporal fusiform cortex, and hippocampus (Pattinson et al., 2009)).

The recorded P_{ET}CO₂ time series were shifted by 3 seconds, to account for the time it takes for the blood to travel from the lungs to the brain tissue. Also, the time-to-peak values of the two basis functions employed in our analysis (see Section 2.2.2), which reflects the delay of the response of the vasculature to changes in PaCO₂, are 4.3 and 9.4 seconds, respectively. Therefore, the range of total delay between the P_{ET}CO₂ and BOLD times-series assumed in our analysis is in a broad agreement with other studies in the literature (Murphy et al., 2011; Panerai et al., 2000; Poulin et al., 1996; Wise et al., 2004).

2.2.2. Mathematical modelling

Dynamic CO₂ reactivity was assessed using linear (impulse response) and non-linear (Volterra kernel) models. In this context, we employed the discrete time Volterra Model (DVM) for a Q -th order non-linear system, which is given by

$$y(n) = \sum_{q=0}^Q \sum_{m_1} \dots \sum_{m_q} k_q(m_1, \dots, m_q) x(n - m_1) \dots x(n - m_q), \quad (1)$$

where $y(n)$ denotes the output (i.e. %BOLD change) and $x(n)$ the input (i.e. P_{ET}CO₂ change) of the system at time n , respectively, $k_q(m_1, \dots, m_q)$ denotes the q -th order Volterra kernel of the system, and Q denotes the model order.

When $Q = 1$, the right-hand side of (1) reduces to the convolution between the input and the first order Volterra kernel, $k_1(m_1)$, which corresponds to the impulse response of a linear system describing the linear effect of the past input values on the output. Similarly, when $Q = 2$, in addition to the linear term, the right-hand side of (1) consists of a nonlinear term that corresponds to the nonlinear second-order convolution between the input and the second order Volterra kernel, $k_2(m_1, m_2)$, which describes the effect of pairwise interactions (products) of past input values on the output.

The Volterra kernels can be estimated efficiently from the input-output data using a functional expansion technique in terms of an orthonormal basis set (Marmarelis, 1993), which is given by

$$k_q(m_1, \dots, m_q) = \sum_{j_1=0}^L \dots \sum_{j_q=j_{q-1}}^L c_{j_1 \dots j_q} b_{j_1}(m_1) \dots b_{j_q}(m_q), \quad (2)$$

where $\{b_j(m); j = 0, \dots, L; m = 0, \dots, M\}$ is a set of $L + 1$ orthonormal basis functions, c_j is the unknown expansion coefficient of the j -th order basis function, and M the memory of the system. Combining (1) and (2), the DVM can be re-expressed in a compact matrix form as

$$\mathbf{y} = \mathbf{V}\mathbf{c} + \boldsymbol{\varepsilon}, \quad (3)$$

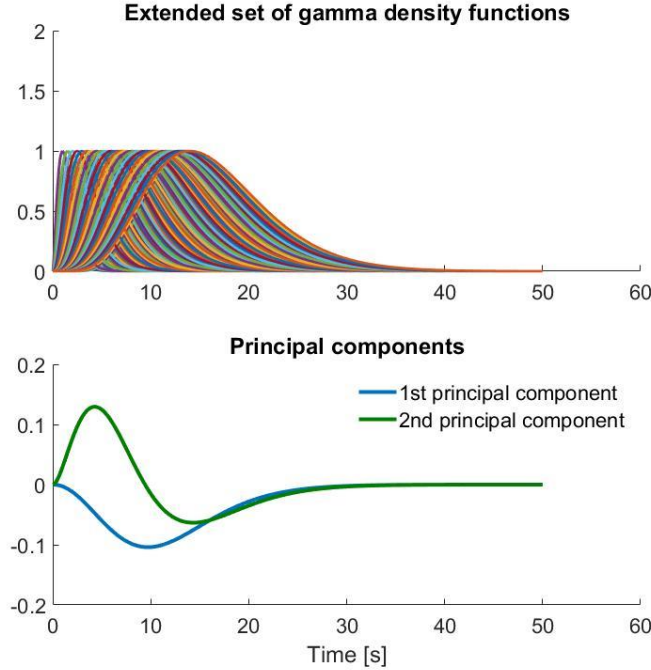


Fig. 2. (top panel) Extended set of gamma basis functions. The location of the peak and the memory of each function were varied in accordance to the dCVR curves obtained with the Laguerre basis in large functionally and structurally defined ROIs. (bottom panel) Reduced set of orthonormal functions, which account for 90% of the variance of the extended set, produced using singular value decomposition. The two orthonormal functions forming the reduced set were used as basis functions in (2) for modeling dCVR.

where \mathbf{V} denotes a matrix the values of which are convolutions of the input with the basis functions. The vector \mathbf{c} of the unknown expansion coefficients can be estimated using ordinary least squares

$$\hat{\mathbf{c}}_{\text{LSE}} = [\mathbf{V}^T \mathbf{V}]^{-1} \mathbf{V}^T \mathbf{y}. \quad (4)$$

A critical issue arising in the application of the functional expansion technique is the proper choice of the basis set, as it may considerably influence the final estimates. In this work, dCVR was initially investigated within large ROIs using the first ($Q = 1$) and second ($Q = 2$) order DVM, where the unknown values of the Volterra kernels were estimated by employing a set of Laguerre basis functions. The Laguerre basis has been extensively used in the literature, particularly in the case of physiological systems, as they constitute a complete set in $[0, \infty)$ and they exhibit exponentially decaying behavior, which makes them a suitable choice for modeling causal, finite-memory systems (Marmarelis, 2004). The j -th order discrete time Laguerre function is given by

$$b_j(m) = \alpha^{(m-1)/2} (1 - \alpha)^{1/2} \sum_{k=0}^L (-1)^k \binom{m}{k} \binom{j}{k} \alpha^{j-k} (1 - \alpha)^k, \quad (5)$$

where α ($0 < \alpha < 1$) is a parameter that determines the rate of exponential decline of these functions, with larger values corresponding to slower decay.

Table 1. The p -values corresponding to the statistical comparison between the NMSE values achieved by a linear ($Q=1$) and non-linear ($Q=2$) DVM, in different ROIs. Statistical comparisons were performed using the Kruskal-Wallis nonparametric one-way ANOVA test.

BRAIN REGION	Dynamic end-tidal forcing	Normal Breathing
Kölliker-Fuse / parabrachial group	0.86	0.86
Anteroventral thalamic nucleus	0.27	0.53
Ventrolateral thalamic nucleus	0.49	0.45
Ventral posterior lateral thalamic nucleus	0.53	0.82
Cerebellum	0.42	0.86
Temporal fusiform cortex	0.45	0.53
Cingulate gyrus	0.39	0.45
Hippocampus	0.60	0.82

The values for the model order (Q) and number of Laguerre functions (L) used in the model, and the parameter α were selected based on model performance, which was assessed in terms of the normalized mean squared error (NMSE) between the measured output (i.e. %BOLD change) and the model prediction given by (1). To prevent overfitting, particularly in the case of normal breathing (resting state) BOLD measurements where the SNR is considerably lower, the range for L and α were selected to be $2 < L < 6$, and $0 < \alpha < 0.6$ respectively. The comparison of the NMSE values suggested that the dynamic relation between CO_2 and BOLD is mainly linear (i.e. $Q = 1$), for both experimental conditions (p -values are shown in Table 1). Therefore, in the following, we present results obtained using linear (impulse response) dynamic models.

Our main purpose was to estimate dCVR curves at single voxels, where the SNR is lower. To this end, we constructed a custom, reduced basis set based on gamma density functions, which have been widely used to model the hemodynamic response function (HRF) (Friston et al., 1998). We considered gamma pdfs as described in (Hossein-Zadeh et al., 2003; Knuth et al., 2001) given by

$$h(t; \tau, \sigma) = \begin{cases} \exp\{-t\sqrt{\sigma \cdot \tau}\} \left(\frac{e \cdot \tau}{\tau}\right)^{\sqrt{\tau/\sigma}} & , \tau \geq 0 \\ 0 & , \tau < 0 \end{cases} \quad (6)$$

where τ and σ determine the location of the peak and width, respectively. Guided by the range of linear (impulse response) dynamics between P_{ETCO_2} and BOLD that were initially estimated in the larger ROIs using the Laguerre basis functions, we constructed an extended set of gamma functions by varying τ and σ to span the entire range of the CVR dynamics observed in different brain regions (Fig. 2 – top panel). Subsequently, we applied singular value decomposition (SVD) on this extended set to obtain a reduced set of orthonormal functions that account for the major fraction of the variability in this set. The results yielded two singular vectors (Fig. 2 – bottom panel), as it was found that the two absolutely largest singular values accounted for more than 90% of the extended set variability.

For both the ROI and voxel-specific analyses, the dCVR curve estimates were obtained using equations (1)-(4) along with the set of two functions of Fig. 2 (bottom panel). For the voxel-specific analysis, we constructed maps of

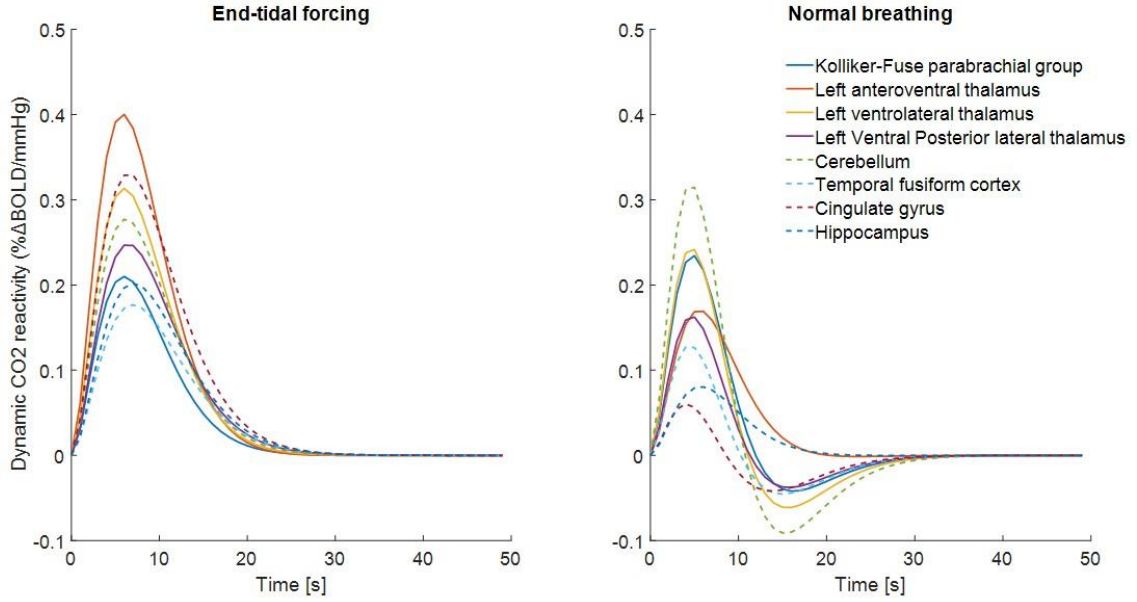


Fig. 3. Dynamic cerebrovascular reactivity (dCVR) curves in different anatomically and functionally defined ROIs during forcing (left panel) and resting (right panel) conditions, obtained using the reduced gamma function basis set (Fig. 2 – bottom panel). The regional variability of dCVR in amplitude and time-to-peak within the same condition, as well as the overall different dCVR shape between the two conditions are evident. Specifically, the undershoot observed during normal breathing is absent during forcing conditions.

the key features of the voxel-specific dCVR, such as area, peak and time-to-peak values, which illustrate the variability of dCVR across the brain. The area of the dCVR curve corresponds to the steady state CVR value that is typically used as an index of CO_2 reactivity in the literature (e.g. Yezhuvath et al. 2009). The peak value describes the maximum instantaneous CO_2 reactivity. The power corresponds to the dCVR curve sum-of-squares, and the time-to-peak corresponds to the time lag of the maximum instantaneous CO_2 reactivity and may be used to assess how fast a particular voxel/ROI responds to CO_2 changes.

In addition, we also performed cluster analysis on the shape of the voxel-wise dCVRs, using unsupervised clustering (k-means) along with the silhouette criterion for selecting the optimal number of clusters in each case (Kaufman et al., 2005; Rousseeuw, 1987). To perform clustering, the values of the dCVR estimates were normalized to a unit energy function with respect to the sum of squares of all time points (Orban et al., 2014).

3. Results

3.1.1. ROI analysis

Table 1 illustrates the p -values of the Kruskal-Wallis nonparametric one-way ANOVA test between the NMSE values from all subjects achieved by linear and non-linear models, using the DVM with $Q = 1$, and $Q = 2$, respectively, for different ROIs. Both models were identified using the functional expansion technique along with the

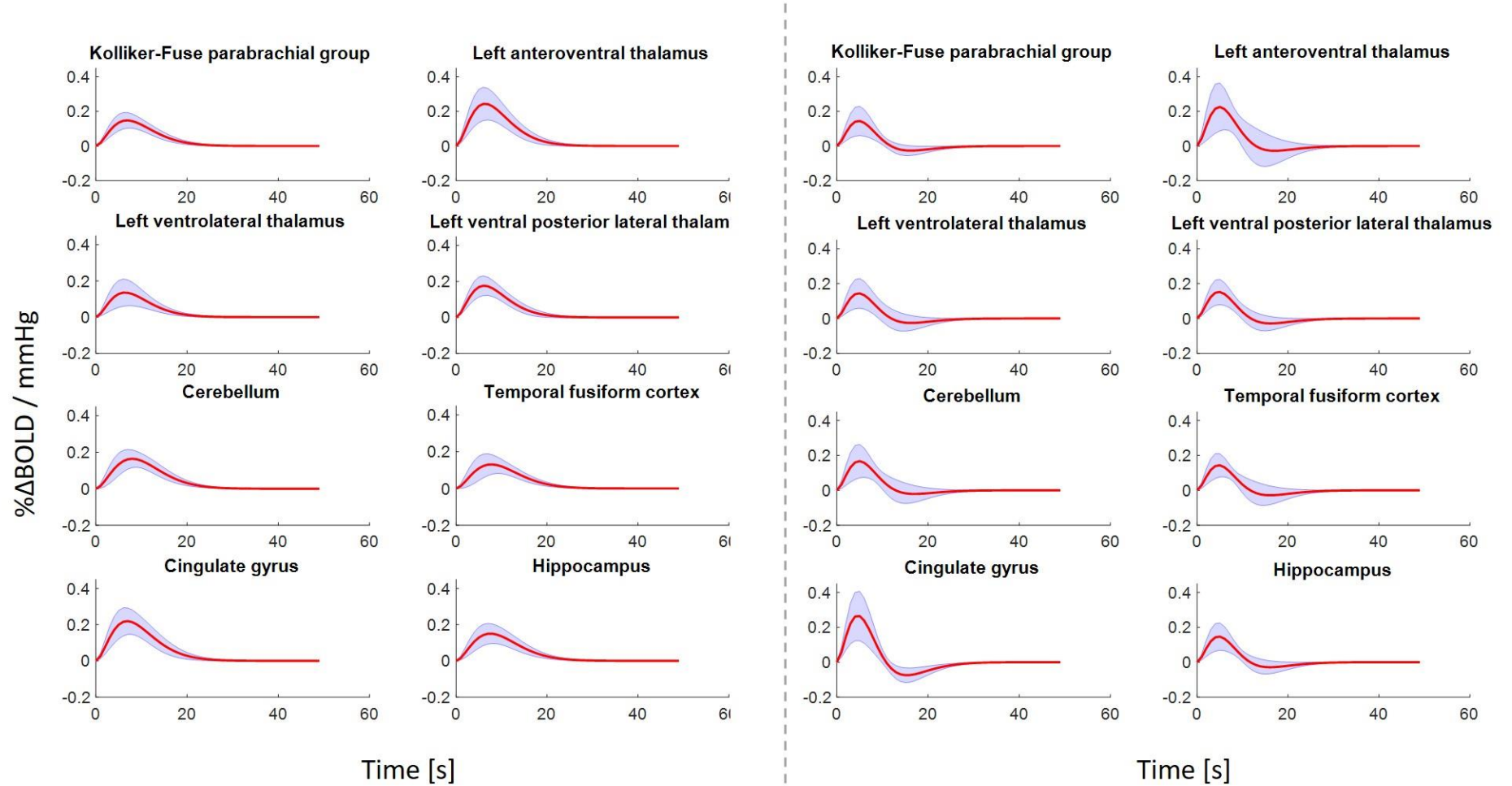


Fig. 4. Average dCVR curves within each ROI across subjects. The red curve corresponds to the mean dCVR curve across all subjects. The blue shaded area corresponds to the standard deviation of the dCVR curve across subjects. Similarly to the individual subject results shown in Fig. 3, the average dCVR curves across subjects reveal that the undershoot observed during normal breathing is largely absent during forcing conditions.

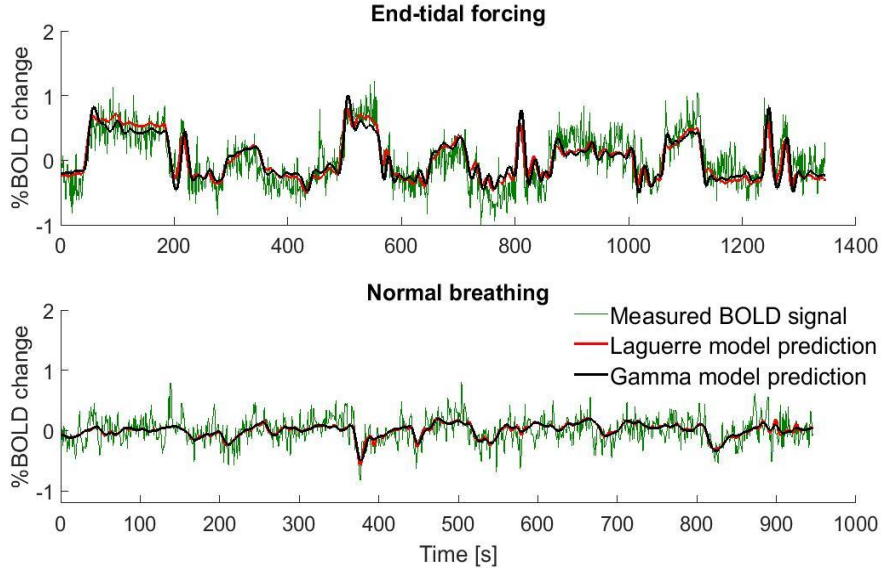


Fig. 5. Representative gamma and Laguerre model output predictions for the left anteroventral nucleus of the thalamus functional ROI during end-tidal forcing (top panel) and resting breathing (bottom panel) conditions. The gamma and Laguerre models yielded similar model predictions, which explained a large fraction of the slow variations in the BOLD signal during end-tidal forcing and normal breathing (resting state conditions).

Laguerre basis. In this context, the null hypothesis was that the NMSE values obtained from both models originate from the same distribution. The p -values suggest that we could not reject the null hypothesis, implying that the dynamic relation between $P_{ET}CO_2$ and %BOLD is predominantly linear for both experimental conditions.

Representative dCVR curves within different ROIs from one individual subject are shown in Fig. 3. The initial part of the dCVR curves suggests a similar response to spontaneous and externally induced larger CO_2 changes; however, the curves corresponding to resting conditions exhibited a more pronounced late undershoot, which is largely absent from the forcing curves (see also the voxel-wise results below). Similar dCVR curve shapes under forcing and resting conditions were observed at the group level as well (Fig. 4). Representative model output predictions achieved using the gamma and Laguerre basis sets for the left anteroventral nucleus of the thalamus functional ROI under end-tidal forcing and normal breathing (resting state) conditions are illustrated in Fig. 5. The gamma and Laguerre models yielded similar model predictions, explaining a large fraction of the slower variations in the BOLD signal during end-tidal forcing and normal breathing.

The estimated dCVR curves in the selected ROIs varied significantly across subjects, with respect to their area and time-to-peak values (Fig. 6). For all functional and structural ROIs, the area and time-to-peak values of the forcing dCVR curve estimates were found to be significantly larger than those under resting conditions. During forcing conditions, structural ROIs exhibited overall larger time-to-peak values compared to functional ROIs, with some differences being statistically significant. In particular, the time-to-peak values of the cerebellum (CB) and temporal fusiform (TFus) cortex were significantly larger to those of the left anteroventral (LAV), left ventrolateral (LVL), and left ventral posterior lateral (LVPL) thalamic nuclei (Fig. 6; bottom left panel). Also, under forcing conditions, both functional (LAV) and structural (cingulate gyrus (CG)) ROIs exhibited significantly larger area values compared to

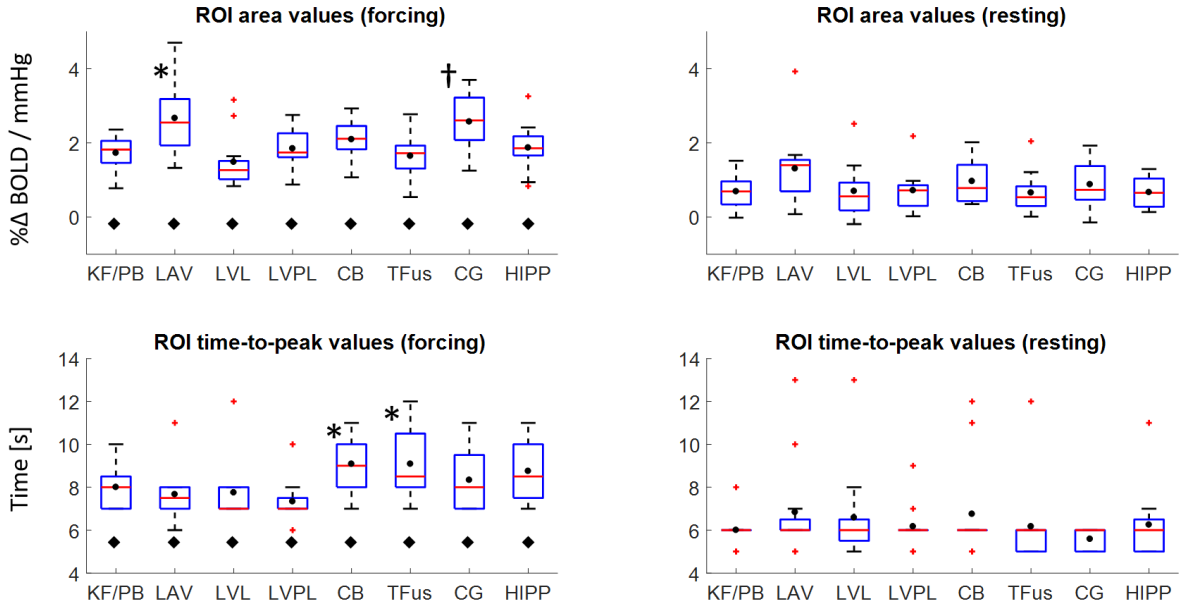


Fig. 6. Box plots of dCVR area and time-to-peak values obtained from the ROI analysis across all subjects, under forcing (left column) and normal breathing (right column) conditions. The red horizontal bars and black circles represent median and mean values, respectively. Under forcing conditions, the LAV and CG exhibited significantly higher area values compared to the KF/PB, LVL, LVPL, TFus, and HIPP ROIs (top left panel: *,† - $p < 0.05$; Kruskal-Wallis nonparametric one-way ANOVA test). Also, the CB, and TFus exhibited significantly higher time-to-peak values compared to the LAV, LVL, and LVPL ROIs (bottom left panel: * - $p < 0.05$). No significant differences between the area and time-to-peak values of any ROIs were observed during resting conditions. The forcing dCVR area and time-to-peak values across all subjects were found to be larger compared to their resting dCVR counterparts for all ROIs (left panels: ♦ - $p < 0.05$). KF/PB: Kolliker-Fuse parabrachial group, LAV: left anteroventral thalamus, LVL: left ventrolateral thalamus, LVPL: left ventral posterior lateral thalamus, CB: cerebellum, TFus: temporal fusiform cortex, CG: cingulate gyrus, HIPP: hippocampus.

other ROIs, including the Kolliker-Fuse parabrachial group (KF/PB), LVL, LVPL, TFus, and hippocampus (HIPP) (Fig. 6; top left panel).

3.1.2. Voxel-wise analysis

Average maps across subjects of voxel-specific features extracted from the corresponding dCVR curves are shown in Fig. 7. The extracted features include area (steady-state CVR), time-to-peak, peak, and power. The area maps obtained under forcing conditions generally exhibit higher intensity values compared to the maps obtained under resting conditions. Overall, subcortical structures such as the thalamus and the brainstem, as well as regions in the cerebral cortex show increased sensitivity to CO_2 challenges. In contrast, WM shows lower sensitivity under both forcing and resting conditions. Under forcing conditions, periventricular WM regions exhibit considerably smaller steady-state CVR values (Fig. 7a). The time-to-peak maps, in which lower intensity values correspond to faster response, show that for many regions in the brain the timing of the maximum instantaneous amplitude of dCVR is generally slower during forcing conditions (Fig. 7c-d).

One-way, nonparametric statistical comparisons between the dCVR feature maps obtained under end-tidal forcing and resting conditions are shown in Fig. 8. The results reveal significant differences ($p_{TFCE} < 0.001$) in the anterior

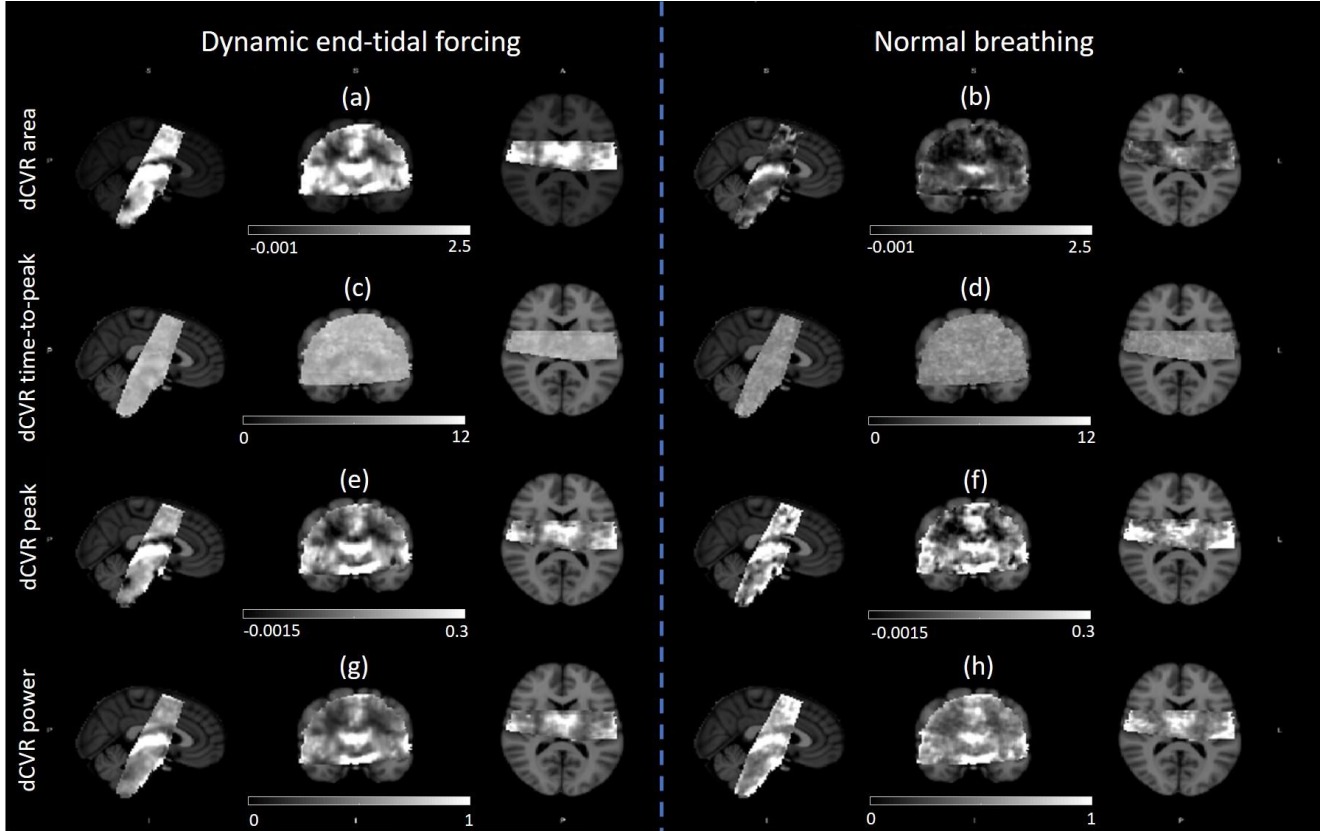


Fig. 7. Average regional maps across subjects of voxel-specific dCVR features during end-tidal forcing (left column) and normal breathing (right column) conditions superimposed on the MNI 152 standard template. First row (a,b): dCVR area. This feature corresponds to the steady-state CVR value. Second row (c,d): dCVR time-to-peak. This feature corresponds to the time lag of the maximum instantaneous effect of CO_2 on the BOLD signal. Third row (e,f): Peak dCVR value. This feature corresponds to the maximum instantaneous effect of CO_2 on the BOLD signal. Fourth row (g,h): dCVR power values. This feature corresponds to the dCVR curve sum-of-squares. Under forcing conditions, the area, peak and power maps exhibit similar patterns of feature variability across different brain regions, revealing increased sensitivity to CO_2 challenges in areas such as the brainstem, thalamus and cerebral cortex. Under resting conditions, the area maps exhibit lower area values possibly due to the late undershoot of the dCVR curve, which decreases its area. WM is generally less sensitive to the CO_2 challenges compared to GM, with periventricular WM regions exhibiting the lowest sensitivity. The time-to-peak maps show that the timing of the maximum instantaneous peak value of dCVR is slower during forcing conditions, suggesting that CO_2 reactivity to larger CO_2 challenges is slower compared to spontaneous fluctuations.

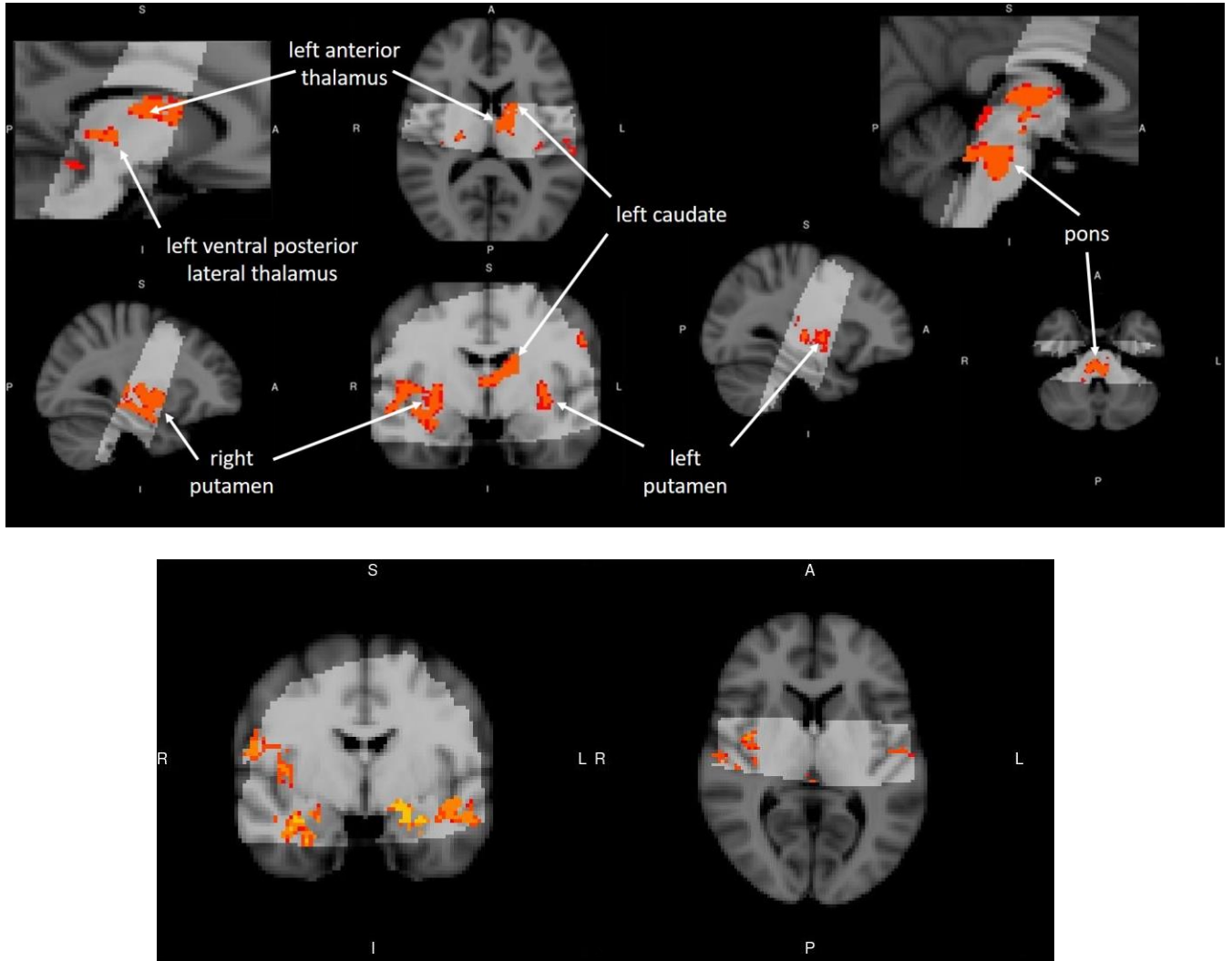


Fig. 8. One-way, nonparametric statistical comparisons (permutation paired test (Winkler et al., 2014)) of the dCVR feature values at each voxel between end-tidal forcing and resting conditions, after registration of the individual feature maps to the MNI standard space. The overlapping area scanned across subjects is shown in lighter gray scale. In all cases the voxels corresponding to significantly different feature values ($p < 0.001$) between end-tidal forcing versus resting conditions are colored. All p -values were corrected using the TFCE method (Smith and Nichols, 2009). Upper panel: dCVR area. Lower panel: dCVR time-to-peak. The comparisons of the area maps (upper panel) show significant differences in the left anterior nuclei, and the left ventral posterior lateral nuclei of the thalamus. They also revealed increased sensitivity in the pons and the putamen. In contrast, the comparison of the time-to-peak maps (lower panel) revealed significant differences in cortical regions, including the insular and temporal fusiform cortices. Note that no areas exhibiting significantly larger dCVR area and time-to-peak values during resting fluctuations, as compared to forcing conditions, were detected.

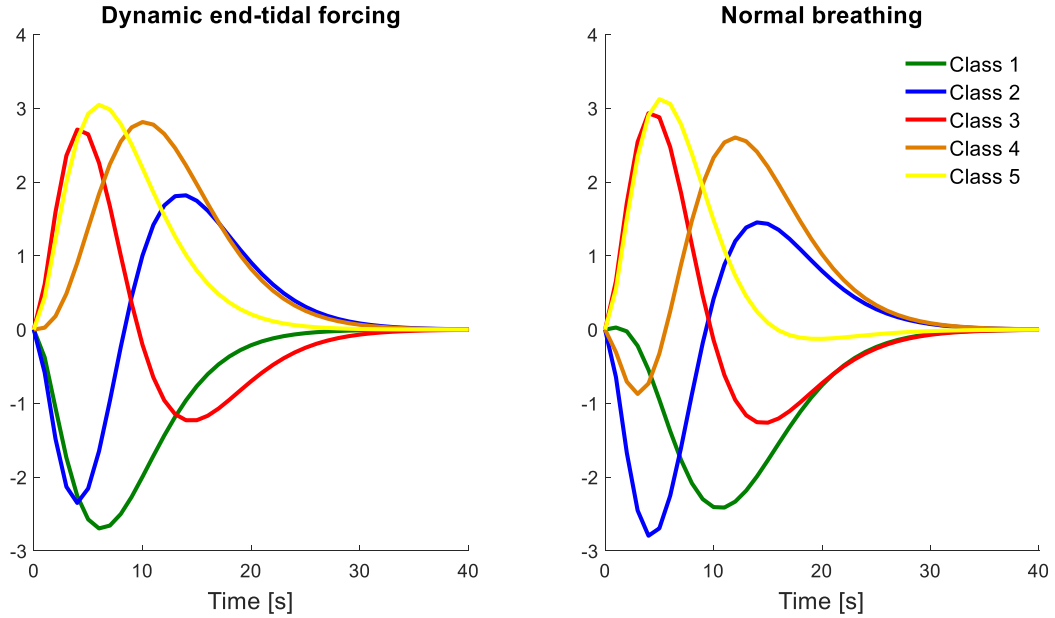


Fig. 9. Mean dCVR curves of clusters obtained using k-means clustering and the silhouette criterion for selecting the optimal number of classes of voxel-specific dCVR curves obtained from a representative subject. Left panel: End-tidal forcing. Right panel: normal breathing. The cluster indices were selected so that mean dCVR curves that are overall more negative correspond to a smaller index values, whereas mean dCVR curves that are overall more positive correspond to larger index values.

and ventral posterior lateral nuclei of the thalamus, the left caudate, the left and right putamen, and the pons. In contrast, the comparison of the time-to-peak maps revealed significant differences ($p_{TFCE} < 0.001$) mostly in cortical regions, including the insular and temporal fusiform cortices. No significant differences were detected for the voxel-wise dCVR peak and power values. Also, no areas yielded significantly larger values for any of the features (area, time-to-peak, peak, power) during resting fluctuations compared to CO₂ challenges.

3.1.3. Clustering analysis

Table S1 in the supplementary material illustrates the number of clusters that resulted from the classification analysis of the dCVR curve shapes. For all subjects, the optimal number of clusters varied between four and five. Fig. 9 shows the mean dCVR curve of each cluster that resulted from the clustering analysis of voxel-specific dCVR curves obtained from a representative subject. The cluster indices were selected so that mean dCVR curves that are overall more negative correspond to a smaller index values whereas mean dCVR curves that are overall more positive correspond to greater index values. Tables S4 and S5 in the supplementary material show the predominant dCVR cluster in the ROIs, which is defined as the cluster with the highest percentage of voxels within each ROI. Under forcing conditions, the vast majority of the ROI voxels was classified into the cluster with the highest cluster index value (4 or 5). This implies that the predominant dCVR curve was unimodal and positive. This result was highly reproducible across subjects. On the other hand, under resting conditions, most of the ROI voxels were classified into cluster 3 (see Fig. 9). The predominant dCVR cluster curve in this case was bimodal, consisting of a large overshoot

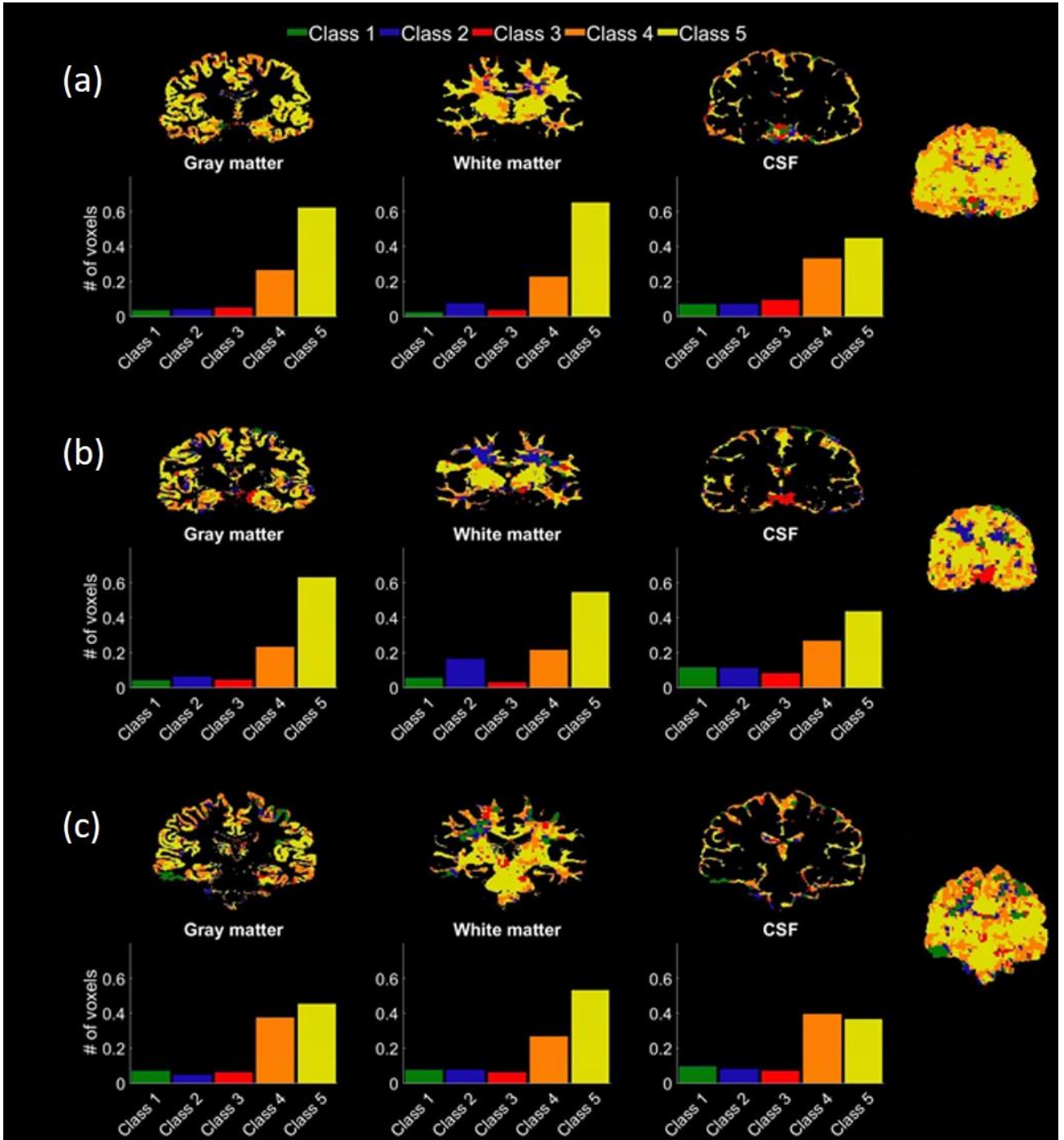


Fig. 10. Representative maps of the cluster spatial distribution within the GM, WM, and CSF anatomical ROIs as well as the entire brain volume for 3 representative subjects during end-tidal forcing conditions. The three representative subjects are shown in (a), (b) and (c) respectively. Smaller cluster index values correspond to more negative dCVR curve shapes, whereas higher index values correspond to more positive dCVR curve shapes. Representative dCVR cluster means are shown in Fig. 9(a). The histogram below each anatomical ROI map displays the distribution of ROI voxels into the clusters formed after application of the clustering analysis. The histograms were normalized with respect to the total number of voxels in each anatomical ROI. The percentage of voxels falling in each cluster for each representative subject is given in Table S2 in the supplementary material. The vast majority of voxels in GM were classified in cluster 5. Similarly, the majority of voxels in WM were classified in cluster 5; however, the proportion of voxels classified into cluster 2 was increased compared to GM. In CSF regions, the proportion of voxels classified in cluster 5 was decreased compared to GM and WM, whereas the proportion of voxels classified in clusters 1-3 was increased.

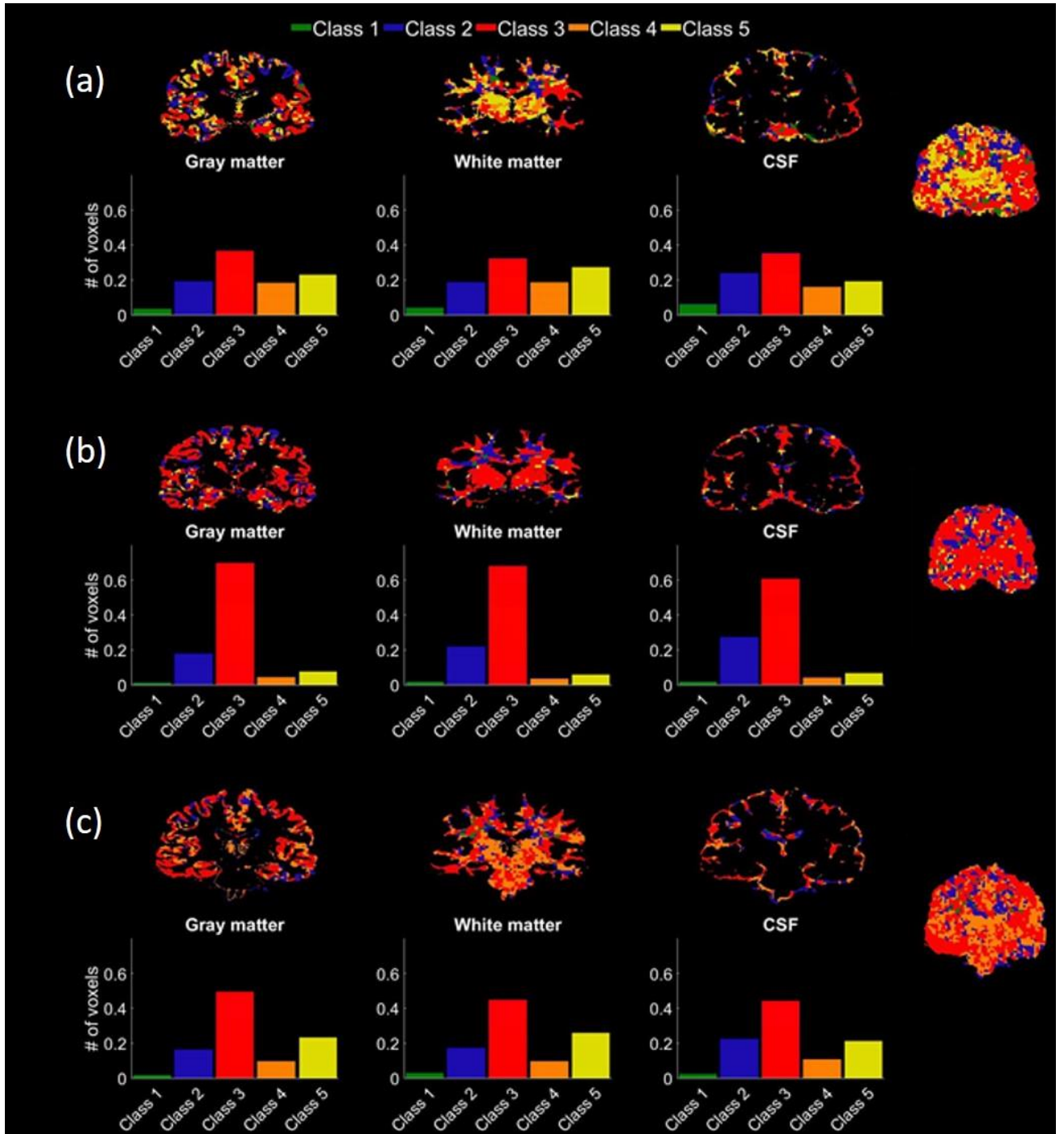


Fig. 11. Representative maps of the cluster spatial distribution within the GM, WM, and CSF anatomical ROIs as well as the entire brain volume for 3 representative subjects during normal breathing (resting state) conditions. The three representative subjects are shown in (a), (b) and (c) respectively. Smaller cluster index values correspond to more positive dCVR curve shapes, whereas higher index values correspond to more positive dCVR curve shapes. Representative dCVR cluster means are shown in Fig. 9(b). The histogram below each anatomical ROI map displays the distribution of ROI voxels into the clusters formed after application of the clustering analysis. The histograms were normalized with respect to the total number of voxels in each anatomical structure. The percentage of voxels falling in each cluster for each representative subject is given in Table S3 in the supplementary material. The vast majority of voxels in all structures were classified into cluster 3, which corresponds to dCVR curve shapes characterized by an early overshoot followed by a late undershoot.

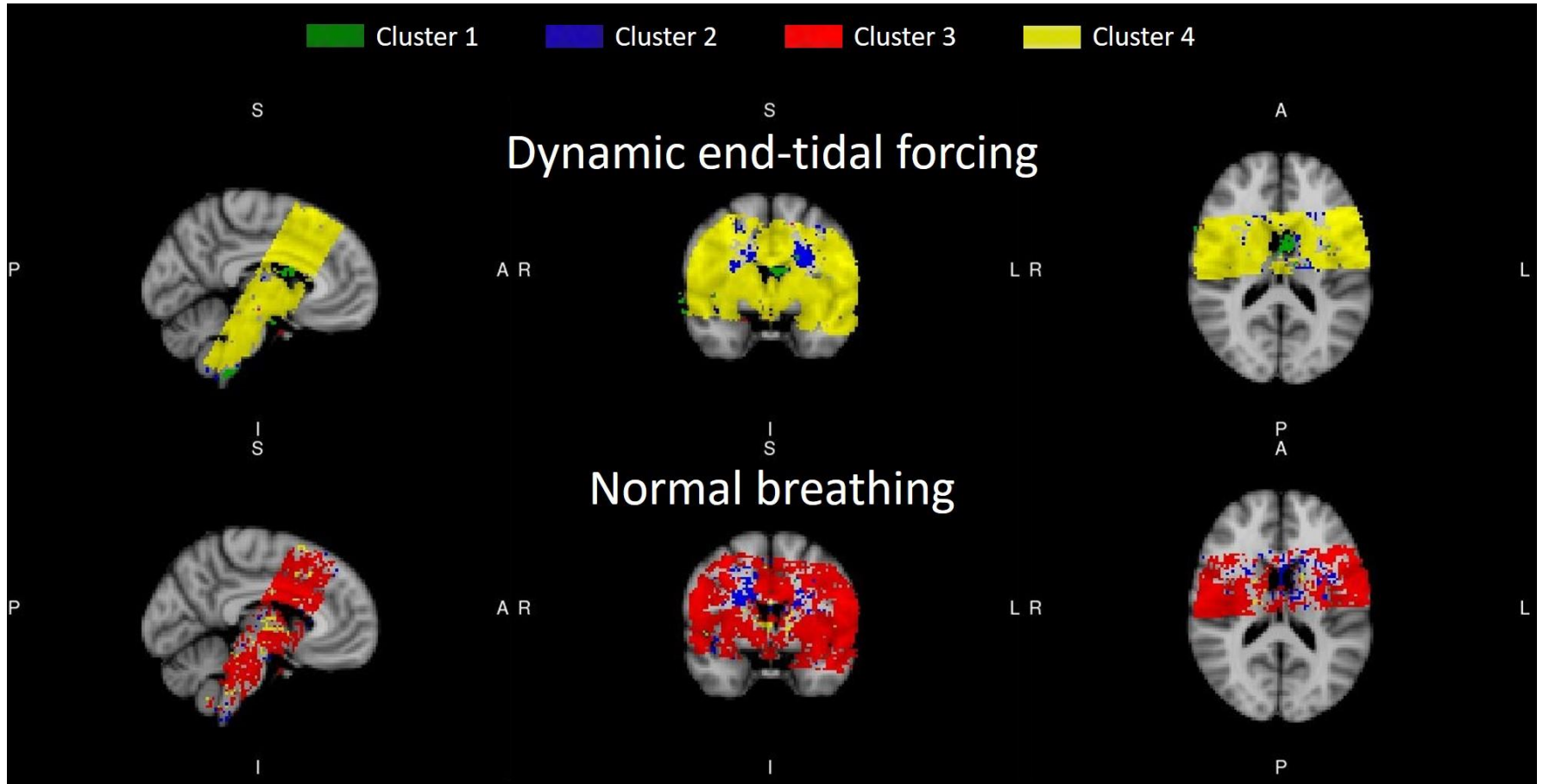


Fig. 12. Reproducibility of the spatial distribution of each dCVR cluster during end-tidal forcing (a) and normal breathing (b) conditions. The voxels (MNI space) that were assigned in the same cluster for at least 6 subjects are shown. Smaller cluster index values correspond to more negative dCVR curve shapes, whereas higher index values correspond to more positive dCVR curve shapes. Representative cluster means are shown in Fig. S1 in the supplementary material. Under forcing conditions, the vast majority of voxels was consistently (across subjects) classified into cluster 4, which corresponds to unimodal curves with a large positive overshoot, for most subjects. Voxels in periventricular regions were consistently classified into cluster 2, which corresponds to bimodal curves with a large negative undershoot followed by a small positive overshoot, for most subjects. Ventricular voxels were classified into cluster 1, which corresponds to unimodal curves with a large negative undershoot, for most subjects. On the other hand, under resting conditions the vast majority of voxels was consistently classified in cluster 3, which is characterized by a large overshoot followed by a late undershoot, for most subjects.

followed by a late, smaller undershoot. However, in the latter case the dominant dCVR cluster in each ROI was found to be less consistent across subjects as compared to forcing conditions, possibly due to the lower SNR.

During end-tidal forcing (Fig. 10), the majority of GM voxel-specific dCVR responses to step CO₂ challenges were classified into cluster 5. In WM, while most of the voxel-specific dCVR responses were classified into cluster 5, the number of voxels classified into cluster 2 was higher compared to GM. This suggests that WM has more voxels responding with an initial undershoot to step CO₂ challenges compared to GM. This effect is more pronounced in CSF-rich regions, where, in comparison to GM, the number of voxel-specific dCVR curves classified into cluster 1 was found to be lower and the number of voxel-specific dCVR curves classified into clusters 1-3 was found to be higher. During normal breathing (Fig. 11), on the other hand, the largest proportion of voxel-specific responses were classified into cluster 3, which corresponds to dCVR curve shapes characterized by an early overshoot followed by a late undershoot. This explains the form of the dCVR shapes obtained for larger ROIs shown in Fig. 3.

The reproducibility of the spatial distribution of each dCVR cluster across subjects during each condition is shown in Fig. 12. Spatial comparison of dCVR clusters across subjects requires an equal number of clusters for all subjects. As the optimal number of clusters identified across subjects and experimental conditions (resting/forcing) varied between 4 and 5 (Table S1 in the supplementary material), clusters with high inter-cluster similarity were merged together to form 4 dCVR curve clusters for all subjects and experimental conditions. The inter-cluster similarity between the dCVR clusters was evaluated in terms of the pointwise Euclidean distance between the centroid (mean dCVR curve) of each cluster. This resulted into clusters 4 and 5 being merged together in all cases, as their mean dCVR curves were found to be the most similar among all clusters. Representative cluster means are shown in Fig. S1 in the supplementary material. Fig. 12 shows the voxels (MNI space) that were assigned to the same cluster in at least 6 subjects. For most subjects, under forcing conditions the vast majority of voxels was classified into cluster 4. Also, voxels in periventricular regions were consistently classified into cluster 2, while ventricular voxels were classified into cluster 1. On the other hand, under resting conditions the vast majority of voxels was classified into cluster 3 for most subjects.

4. Discussion

We investigated the regional variability of dCVR by modeling the dynamic interactions between CO₂ and BOLD in healthy subjects during resting conditions and hypercapnic step changes induced by dynamic end-tidal forcing. To this end, we employed an efficient systems identification technique (functional expansions) to obtain estimates of dCVR curves within single voxels over the entire scan field of view, and larger ROIs possibly involved in the brainstem respiratory control network, whereby we constructed a custom basis set by using the Laguerre and gamma basis sets (see Section 2). Based on this, we demonstrated that dCVR exhibits significant regional variability both with respect to its particular features (Fig. 7), as well as with respect to its shape (Figs. 10-12), which suggest the dynamic effect of CO₂ on the BOLD signal strongly depends on brain region and experimental condition. Our results suggest that the proposed methodology yields robust dCVR estimates in single voxels even during resting conditions, despite the low SNR associated with the latter. This has important implications, as it suggests that it is feasible to obtain reliable dCVR curve estimates without the need of externally induced stimuli (end-tidal/prospective forcing, controlled breathing).

This line of research yields promise, including the clinical setting, as it may lead to protocols which are easier to implement and applicable to a potentially wider class of patient populations with disorders associated with cerebrovascular dysfunction. Such disorders include arterial stenosis (Mandell et al., 2008b) and occlusion (De Vis et al., 2015), enhanced risk of stroke (Gur et al., 1996; Markus, 2001; Silvestrini et al., 2000), steno-occlusive diseases such as Moyamoya disease (Donahue et al., 2013; Mikulis et al., 2005), small-vessel diseases (Conklin et al., 2011,

2010) and Alzheimer's disease (Marmarelis et al., 2016, 2013; Silvestrini et al., 2011). Beyond cerebrovascular diseases, we speculate that modeling dCVR within structures involved in central chemoreception could provide valuable insight towards understanding and treating diseases associated with respiratory control. Altered chemoreception has been associated with obstructive sleep apnea (Kaw et al., 2009; Mokhlesi and Tulaimat, 2007; Wang et al., 2007), the central hypoventilation syndrome (Dubreuil et al., 2008; Guyenet et al., 2010; Shea et al., 1993), and multiple system atrophy (Benarroch et al., 2007; Gaig and Iranzo, 2012). Future research is required to test the clinical utility of these techniques, potentially in tandem with other complimentary techniques to understand the human brainstem (Ezra et al., 2015; Faull et al., 2015; Faull and Pattinson, 2017; Vinet and Zhedanov, 2010).

4.1.1. The resting-state dCVR late undershoot

Our analysis revealed that under resting conditions the estimated dCVR curves exhibited a late undershoot that was absent during dynamic end-tidal forcing conditions (Fig. 3). A potential explanation of this observation could be a reduction in compliance reserve associated with the raised mean $P_{ET}CO_2$ baseline during CO_2 challenges. This rise in mean $P_{ET}CO_2$ was a result of both the increase in $P_{ET}CO_2$ baseline by 1 mmHg above the subjects' natural $P_{ET}CO_2$ needed for the system to function correctly, as well as the step CO_2 challenges that were delivered to the subjects (Section 2.1.1). Previous studies have shown that each 1 mmHg increase or decrease in $PaCO_2$ over the range of 20–60 mmHg produces a CBF change of same direction of approximately 1–2 ml/100 g/min, or 2.5% (Ide et al., 2003; Poulin et al., 1996). During forcing conditions, the recorded rise in mean $P_{ET}CO_2$ was approximately 3.4 mmHg (due to the hypercapnic steps), which would increase mean CBF by approximately 7 to 16% (Pattinson et al., 2009).

The reduction in compliance reserve caused by such an increase in mean $P_{ET}CO_2$ can be described using the arteriolar compliance model of CBF response to a vasoactive stimulus developed in (Behzadi and Liu, 2005). Although this model was initially developed for neuronal inputs, its basic idea can be generalized to any input that triggers a vasoactive signaling cascade, such as CO_2 , without any loss of generality. CO_2 is believed to contribute to the development of pH gradient across arteriolar walls, and both CO_2 and pH regulate cerebrovascular contractility (Kontos et al., 1977a, 1977b; Lassen, 1968; Yoon et al., 2012). However, the precise molecular mechanisms regulating this chemosensitivity are still poorly understood.

The arteriolar compliance model is an extension of the (Friston et al., 2000) linear feedback model of the CBF response to a vasoactive signal. According to the arteriolar compliance model, a vasoactive signal modulates arteriolar muscular compliance, which subsequently leads to changes in vessel radius and CBF. Total compliance is defined as the parallel combination of an active and a passive component. The active component represents smooth muscle, whereas the passive component represents connective tissue, such as basal lamina. This results in a non-linear relation between arteriolar radius, which depends on $PaCO_2$, and smooth muscle compliance. A key constituent term of the model is the feedback, which represents mechanisms that attempt to drive CBF back to baseline state shortly after the onset of the stimulus. Such mechanisms can be the action of stretch-mediated receptors in a vessel wall leading to vascular smooth muscle constriction. The feedback term is inversely related to baseline $PaCO_2$. This results from the assumption of a non-linear relation between the radius and compliance of arterioles, and the mathematical derivation of the model.

The reciprocal contribution of $PaCO_2$ in the feedback term can be used to describe the late undershoot of dCVR curves obtained in our work under normal breathing conditions. Specifically, under normocapnia, the feedback term, which tends to drive CBF back to baseline levels shortly after the onset of the stimulus (spontaneous CO_2 fluctuations), is stronger compared with CO_2 challenges. This stronger feedback term results in faster CBF response with a post-stimulus undershoot. On the other hand, during hypercapnic CO_2 challenges, when mean $P_{ET}CO_2$ is elevated compared to normal breathing, the feedback term is weaker. This results in a slower CBF response with minimal post-stimulus undershoot. These results were illustrated in (Behzadi and Liu, 2005) using realistic simulations and agree with the findings in our work, which show a late undershoot in the dCVR curves obtained under normal breathing conditions

that is absent from dCVR curves obtained under forcing conditions.

4.1.2. Variability of dCVR curve features across experimental conditions and brain regions

Resting vs. forcing conditions - ROI analysis: The ROI analysis shown in Fig. 6 revealed significant differences ($p < 0.05$) between the dCVR curve area and time-to-peak values under end-tidal forcing versus normal breathing conditions. No significant differences were detected for the dCVR peak and power values between forcing/resting conditions. Moreover, these significant differences were found in one direction only. Specifically, no ROIs exhibiting larger dCVR area or time-to-peak values for resting breathing compared to end-tidal forcing conditions were found. The main reason for the dCVR area differences is that, under normal breathing conditions, the dCVR curves exhibited a late undershoot, which decreased the overall dCVR curve area. On the other hand, this late undershoot was absent from the dCVR curves obtained under forcing conditions. This is further supported by the dCVR area maps shown in Fig. 7, where it can be seen that dCVR area is larger during forcing compared to resting conditions for almost all voxels, as well as the clustering results (Figs. 10, 11), which revealed that the dominant dCVR clusters during forcing and resting conditions were unimodal (no undershoot) and bimodal, respectively. As a result, the area of the dCVR curves obtained under forcing conditions was found to be overall larger compared to resting conditions.

The differences in the dCVR time-to-peak observed between the two conditions could also be explained by the elevated PaCO_2 baseline and larger magnitude fluctuations that occurred under forcing conditions. According to the (Behzadi and Liu, 2005) arteriolar compliance model, under normal breathing conditions, whereby PaCO_2 baseline is lower, the CBF response to a vasoactive stimulus resolves faster. In contrast, under hypercapnic conditions, whereby the mean P_{ETCO_2} baseline was raised by approximately 3.4 mmHg with respect to resting conditions (Section 4.1.1), the CBF response is overall slower. The large step CO_2 increases induced during forcing conditions may also contribute to larger time-to-peak values, as the cerebral vasculature contracts more passively at elevated baseline states. Therefore, it may require more time to attain its maximum instantaneous responsiveness to larger CO_2 increases.

In contrast, the dCVR peak and power values were not significantly different between dynamic end-tidal forcing and normal breathing conditions, implying that they were not affected significantly by the late undershoot observed under normal breathing. Specifically, the dCVR peak value reflects the maximum instantaneous dCVR response. It does not depend on the late undershoot, which, according to the (Behzadi and Liu, 2005) model, is associated with the baseline CBF state. On the other hand, the dCVR power is defined as the sum of squares of the dCVR curve values. In contrast to the dCVR area, for which the late undershoot observed under resting conditions tends to decrease its overall value, in the case of dCVR power the late undershoot does not change significantly the overall value compared to forcing conditions, as these values are squared when calculating dCVR power.

Apart from significant differences in dCVR features between experimental conditions, our analysis also revealed significant differences in dCVR features between different ROIs within the same condition. Fig. 6 shows that under CO_2 challenges, both functional (left anteroventral thalamus (AV)) and structural (cingulate gyrus (CG)) ROIs exhibited significantly larger area values compared to other ROIs, including the Kolliker-Fuse parabrachial group (KF/PB), left ventrolateral thalamus (VL), left ventral posterior lateral thalamus (VPL), temporal fusiform cortex (TFus), and hippocampus (HIPP) ($p < 0.05$). No significant differences of area values were found between these ROIs under normal breathing conditions.

With regards to the observation that the left AV exhibited higher area values compared to the other functional thalamic ROIs (VL, and VPL), a potential hypothesis is that under forcing conditions there is a larger involvement of the AV nucleus in mediating sensory components of respiration to large cortical regions. This results in higher BOLD signal fluctuations in the AV nucleus compared to the VL and VPL nuclei. This hypothesis is supported by neuroimaging results suggesting that activity in the AV nucleus is more strongly connected with large cortical territories involved in processing of respiratory-related information, such as the frontal and anterior cingulate cortices,

as compared to the VPL nucleus of the thalamus (Evans et al., 2002; McKay et al., 2003; Pattinson et al., 2009; Von Leupoldt et al., 2008). It is also supported by diffusion tractography results, which showed similar connectivity between the VL and VPL nuclei, but distinct connectivity profiles between these nuclei and the AV thalamic nucleus (Pattinson et al., 2009). It is interesting to note that, although the CG was not identified as one of the areas that showed significant activations to the external CO₂ stimuli, it has been implicated in respiratory control due to its strong structural connections to the AV nuclei of the thalamus (Pattinson et al., 2009). We also note that the most important reason for which the CG was not found to be activated in both (Pattinson et al., 2009) and in our analysis (Fig. 8), is perhaps statistical thresholding.

The cerebellum (CB) and TFus exhibited significantly larger time-to-peak values compared to the left VL, left AV, and left VPL thalamic nuclei. We speculate that the faster response delay under forcing conditions of the latter respiratory-related, functionally-defined ROIs compared to the former structurally-defined ROIs could be associated with increased neuronal activity in response to CO₂ challenges.

Resting vs. forcing conditions - Voxel-wise analysis: The statistical comparisons of voxel-specific dCVR area values between resting and end-tidal forcing conditions (Fig. 8) revealed significant differences in the anterior and ventral posterior lateral nuclei of the thalamus, the left caudate, the left and right putamen, and the pons, in agreement with the ROI analysis and the voxel-wise results reported in (Pattinson et al., 2009). In the latter study, these differences were identified using standard fMRI voxel-wise analysis, i.e. convolving the CO₂ stimuli with a standard curve and obtaining a regression coefficient for each voxel. This assumes that the dynamics of the BOLD response to CO₂ changes are identical in all voxels except a scaling factor. As discussed in the same paper (e.g. Fig. 3 in (Pattinson et al., 2009)), the obtained results reflect the slope of the BOLD- $P_{ET}CO_2$ relationship. This is mainly due to that in voxels that are activated, the SNR increases; therefore, linear correlations become stronger. In the present paper, we have applied a dynamic system-theoretical framework to study in detail the voxel-specific dynamics of the BOLD response to CO₂ changes which are quantified by the corresponding dCVR curves. This provides richer information than the analysis presented in (Pattinson et al., 2009) as it allows e.g. for different curve shapes (unimodal/bimodal etc.) and time-to-peak values compared to using a uniform curve across the brain.

Among several possible features that can be extracted from these curves, it was found that the area under the dCVR curve yielded statistically significant differences (permutation paired testing, TFCE correction) between forcing/resting conditions (Fig. 8). Interestingly, the area of the dCVR curve is equivalent to the steady-state CVR response to a unit step change in $P_{ET}CO_2$ (steady-state step response in systems theory terminology), which also corresponds to the standard definition of CVR (Fierstra et al., 2013). The comparison of the voxel-specific dCVR time-to-peak values also revealed significant differences between the two experimental conditions (Fig. 8). These differences were detected mainly in cortical regions, including the insular and temporal fusiform cortices. This implies that, in these regions, the relative time that the cerebral vasculature needs to attain its maximum instantaneous responsivity to changes in PaCO₂ during forcing conditions is longer compared to resting conditions. It is known that in the presence of a hypercapnic stimulus, there is a larger CBF increase relative to baseline CBF in GM structures (especially cortical regions) compared to other structures (Ramsay et al., 1993; Rostrup et al., 2000). As a result, the differences in dCVR time-to-peak between forcing versus resting conditions are larger in GM relative to other structures in the brain.

Dissociating the contribution of neuronal activity and vascular reactivity on the BOLD signal using the data analyzed in this study (and in a more general context) is challenging, particularly during resting conditions, and lies beyond the scope of the present paper. It is worth noting, however, that significant differences in the BOLD response to externally induced CO₂ step challenges compared to normal breathing that are observed in some brain regions, in addition to vascular reactivity, might be due to differences in neural activation (Pattinson et al., 2009). We speculate that these neural activation - induced changes in BOLD that occur in response to CO₂ challenges seem to be (perhaps unsurprisingly) reflected on features depending on the entire shape of the dCVR curve, such as total area, rather than individual measures that only depend on instantaneous values of the dCVR curve, such as peak value. This hypothesis

is supported by the results shown in Figs. 7-11. Specifically, while the increase in dCVR area values during forcing conditions is widespread over the entire FOV and is mostly due to the lack of an undershoot in the dCVR shapes (Figs. 7, 10-11), this increase was more pronounced and hence survived the permutation significance testing in the areas shown in Fig. 8 (upper panel). These areas are similar to the areas identified in (Pattinson et al., 2009) as showing increased sensitivity to the external CO_2 challenges, possibly due to activation of CO_2 sensitive neurons.

4.1.3. The dCVR curve shape and its relation to the underlying anatomy

The clustering analysis of the voxel-wise dCVR estimates (Figs. 9-12) revealed that the dCVR shapes are distributed symmetrically across the brain. In the case of end-tidal forcing (Fig. 10), the largest part of the brain WM and GM was assigned to clusters which corresponded to voxel-specific dCVR curves with more positive curve shapes. On the other hand, in the case of normal breathing (Fig. 11), the prevalence of dCVR curve shapes exhibiting a late undershoot in the brain WM and GM was overall more widespread compared to end-tidal forcing.

During hypercapnia, periventricular WM regions were found to exhibit negative steady-state CVR values (Fig. 7). Similar results were also reported in (Mandell et al., 2008a; Naganawa et al., 2002). In these works, the authors attributed this result to “vascular steal” effects. Negative CVR can be seen more clearly from the clustering of the voxel-specific dCVR curves in the brain WM, shown in Fig. 13, where periventricular WM regions yielded dCVR curves that were classified into clusters characterized by prevalently negative dCVR curves (clusters 1 and 2) compared to the rest of the brain WM. Similarly, CSF-rich regions in the brain, such as the lateral ventricles, yielded a larger proportion of dCVR curves that were classified to clusters characterized by prevalently negative dCVR curves (clusters 1 and 2) compared to GM and WM, as shown by the histograms in Fig. 10. This agrees with the findings of (Thomas et al., 2013), where the ventricular BOLD signal was found to be anti-correlated with hypercapnic step changes in CO_2 , which was attributed to CSF movement due to the large blood volume increase that occurs in response to the large hypercapnic CO_2 step changes.

During resting conditions, the clustering analysis revealed that voxel-specific dCVR curve shapes may be different compared to forcing conditions. Specifically, Figs. 10 and 11 show that the histogram of the cluster indices in each anatomical structure changes between forcing and normal breathing conditions. Therefore, the dCVR curve shape of a particular voxel was found to be different between conditions. This suggests that although the underlying mechanism of vasodilation was found linear in the range of P_{ETCO_2} values examined in this study, it may respond differently to CO_2 fluctuations during normal breathing compared to dynamic end-tidal forcing. We believe that the main reason for the different dCVR shapes is that each experimental condition is associated with a different operating point along the PaCO_2 -BOLD response curve (Tancredi and Hoge, 2013). Moreover, the fact that nonlinear models were not found to significantly outperform linear models implies that for the range of CO_2 changes around the mean $\text{PaCO}_2/P_{\text{ETCO}_2}$ values examined in the present paper, a linear approximation around this operating point is sufficient. Specifically,



Fig. 13. Representative results of the clustering analysis in WM for three representative subjects (same subjects shown in Figs. 9 and 10). While most of the voxels were assigned to clusters 4 and 5, which are characterized by dCVR curves exhibiting a large overshoot, WM periventricular voxels were mainly classified in clusters which are characterized by dCVR curves exhibiting an initial undershoot.

during CO₂ challenges, the recorded rise in mean P_{ET}CO₂ was approximately 3.4 mmHg (Pattinson et al., 2009). This increment in mean P_{ET}CO₂, in its turn, would result in an increase in mean CBF by approximately 7 to 16%. According to the arteriolar compliance model (Behzadi and Liu, 2005) this would have an effect of the shape of the dCVR curve suggesting that the dynamic linear model corresponding to each condition depends on the underlying baseline PaCO₂ (Sections 4.1.1-4.1.2).

The clustering analysis was generally reproducible at the group level as shown in Fig. 12. However, the cluster spatial overlap reduced when considering more subjects. There are two main reasons for this: (i) the misregistration of the individual dCVR maps to the MNI space due to the partial scanning field used in this study, and (ii) the reduction of the number of dCVR clusters into 4 to allow comparisons across subjects, which may be suboptimal for some subjects. Overall, the cluster reproducibility is stronger for the forcing data, due to the higher SNR. However, we note that the difficulty related to registering the limited field of view data to the MNI space affected the reproducibility results.

Similar clustering results were also reported in a recent work by (Champagne et al., 2017). In this work, the authors employed a novel protocol, which involved hyperoxic gas challenges, to obtain step hypercapnia-induced response delay maps calibrated for blood arrival time. The latter were combined with traditional CVR and (non-calibrated) hypercapnia-induced response delay maps to derive clusters of brain regions with distinct CBF characteristics. This analysis allowed the authors to define clusters of voxels with long temporal delays during hypercapnia either due to vascular morphology or dynamic blood flow redistribution. On the other hand, we performed clustering with respect to dCVR curve shapes and we did not explicitly measure the bolus arrival time. Therefore, direct comparison between the two clustering results is not straightforward. Nonetheless, some forcing dCVR curves revealed from our analysis (e.g. those with an initial undershoot followed by a larger overshoot) possibly reflect a delayed response to CO₂ challenges as well. These shapes were mainly associated with cluster 2, which in most subjects overlaps with the voxel clusters with long hypercapnia-induced response delay in (Champagne et al., 2017). However, differentiation of possible causes for the longer temporal delays during CO₂ challenges was not feasible using the data analyzed in our work and remains to be studied in future research.

4.2. Study Limitations

The aim of this study was to model the dynamic interactions between %BOLD signal and PaCO₂. The data analyzed were collected in a previous study aiming to determine the human brainstem respiratory control network (Pattinson et al., 2009). The scanning field comprised 16 oblique coronal slices optimized for imaging the brainstem in high temporal resolution. This restricted the aim of modeling of dCVR curves mainly in subcortical structures including the brainstem and the thalamus and did not allow extension of the analysis in some cortical regions that would enable comparisons across cortical lobes. Moreover, the limited scanning field made registration into a common stereotactic space challenging, which possibly affected the comparison of our results at the group level (Fig. 8). Future work performed using a larger field of view with higher contrast (e.g. (Faull et al., 2015, 2016; Pattinson et al., 2009)) would help overcome these limitations.

During the experiment, subjects wore a face mask that was attached to a breathing system. The baseline of P_{ET}CO₂ time-series acquired during the resting-state experiment were slightly higher (44.43 ± 2.09 mmHg) than what is typically reported in the literature (40-42 mmHg) possibly due to some small amount of rebreathing. However, this should not have affected the results as these baseline values were far from the hypercapnic range (> 50 mmHg). Also, in young healthy subjects, changes in PaCO₂ and PaO₂ are reflected closely in P_{ET}CO₂ and P_{ET}O₂, respectively (Hoskins, 1990; Mark et al., 2011; Robbins et al., 1990). Therefore, as the subjects who participated in this study were healthy and in the young- or mid-age range, we hypothesize that the gradient between PaCO₂ (PaO₂) and P_{ET}CO₂ (P_{ET}O₂) was constant. As dCVR estimates were obtained using variations of P_{ET}CO₂ and BOLD around their mean values, this suggests that using P_{ET}CO₂ was suitable for dCVR estimation in our particular subject group.

Lastly, the respiratory protocol employed in the original study (Pattinson et al., 2009) included challenges raising $P_{ET}CO_2$ up to 5 mm Hg above the subjects' natural $P_{ET}CO_2$. This hypercapnic range of $P_{ET}CO_2$ is at the border between the linear and non-linear regions of the $P_{ET}CO_2$ -BOLD curve (Battisti-Charbonney et al., 2011; Halani et al., 2015; Tancredi and Hoge, 2013), which may have resulted in the selection of linear dynamic models between $P_{ET}CO_2$ and BOLD in our investigation. Therefore, further extension of the present work includes the analysis of data collected over a larger hypercapnic range of $P_{ET}CO_2$ to investigate modeling of non-linear dCVR.

5. Conclusion

In this work, we used linear and non-linear models to investigate dynamic CO_2 reactivity in the human brain during both resting breathing and hypercapnic externally induced step changes in CO_2 , using measurements from 12 healthy subjects. We initially investigated larger ROIs and concluded that in these regions dynamic CO_2 reactivity is mainly linear, for both experimental conditions. Therefore, we rigorously investigated the regional variability of dynamic CO_2 reactivity in individual voxels over the entire scan field of view using linear models. In this context, we estimated voxel-specific dynamic CO_2 reactivity curves, and we showed that the regional characteristics of these curves vary considerably across different brain regions, and that their shape might be different under the two experimental conditions. Finally, we performed clustering analysis on the shapes of the estimated curves, which resulted into clusters of similar curve shapes that were distributed symmetrically across the brain. Our results suggest that it is feasible to obtain reliable estimates of dynamic cerebrovascular reactivity curves from resting-state data, which could allow the design of safer and easier to implement clinical protocols for the assessment of dCVR, which do not require external stimuli (e.g. hypercapnia), in any patient population.

Acknowledgements

This work was supported by the Natural Sciences and Engineering Research Council of Canada (Discovery Grant awarded to GDM) and the Fonds Recherche Nature et Technologies Quebec (Team Grant awarded to GDM). KP is supported by the National Institute for Health Research Oxford Biomedical Research Centre based at Oxford University Hospitals NHS Trust and University of Oxford. KP has acted as a consultant for Nektar Therapeutics. The work for Nektar has no bearing on the contents of this manuscript.

References

- Attwell, D., Buchan, A.M., Charkpak, S., Lauritzen, M., MacVicar, B.A., Newman, E.A., 2010. Glial and neuronal control of brain blood flow. *Nature* 468, 232–243. <https://doi.org/10.1038/nature09613>
- Battisti-Charbonney, A., Fisher, J., Duffin, J., 2011. The cerebrovascular response to carbon dioxide in humans. *J. Physiol.* 589, 3039–48. <https://doi.org/10.1113/jphysiol.2011.206052>
- Behzadi, Y., Liu, T.T., 2005. An arteriolar compliance model of the cerebral blood flow response to neural stimulus. *Neuroimage* 25, 1100–1111. <https://doi.org/10.1016/j.neuroimage.2004.12.057>
- Benarroch, E.E., Schmeichel, A.M., Low, P.A., Parisi, J.E., 2007. Depletion of putative chemosensitive respiratory neurons in the ventral medullary surface in multiple system atrophy. *Brain* 130, 469–475. <https://doi.org/10.1093/brain/awl357>
- Bhagal, A.A., Philippens, M.E.P., Siero, J.C.W., Fisher, J.A., Petersen, E.T., Luijten, P.R., Hoogduin, H., 2015. Examining the regional and cerebral depth-dependent BOLD cerebrovascular reactivity response at 7T. *Neuroimage* 114, 239–248. <https://doi.org/10.1016/j.neuroimage.2015.04.014>
- Blockley, N.P., Driver, I.D., Francis, S.T., Fisher, J.A., Gowland, P. a., 2011. An improved method for acquiring cerebrovascular reactivity maps. *Magn. Reson. Med.* 65, 1278–1286. <https://doi.org/10.1002/mrm.22719>
- Blockley, N.P., Harkin, J.W., Bulte, D.P., 2017. Rapid cerebrovascular reactivity mapping: Enabling vascular

- reactivity information to be routinely acquired. *Neuroimage* 159, 214–223. <https://doi.org/10.1016/j.neuroimage.2017.07.048>
- Bokkers, R.P.H., van Osch, M.J.P., van der Worp, H.B., de Borst, G.J., Mali, W.P.T.M., Hendrikse, J., 2010. Symptomatic carotid artery stenosis: impairment of cerebral autoregulation measured at the brain tissue level with arterial spin-labeling MR imaging. *Radiology* 256, 201–8. <https://doi.org/10.1148/radiol.10091262>
- Bright, M.G., Murphy, K., 2013. Reliable quantification of BOLD fMRI cerebrovascular reactivity despite poor breath-hold performance. *Neuroimage* 83, 559–568. <https://doi.org/10.1016/j.neuroimage.2013.07.007>
- Brugniaux, J. V., Hodges, A.N.H., Hanly, P.J., Poulin, M.J., 2007. Cerebrovascular responses to altitude. *Respir. Physiol. Neurobiol.* 158, 212–223. <https://doi.org/10.1016/j.resp.2007.04.008>
- Champagne, A.A., Bhogal, A.A., Coverdale, N.S., Mark, C.I., Cook, D.J., 2017. A novel perspective to calibrate temporal delays in cerebrovascular reactivity using hypercapnic and hyperoxic respiratory challenges. *Neuroimage* 1–12. <https://doi.org/10.1016/j.neuroimage.2017.11.044>
- Conklin, J., Fierstra, J., Crawley, A.P., Han, J.S., Poubanc, J., Mandell, D.M., Silver, F.L., Tymianski, M., Fisher, J.A., Mikulis, D.J., 2010. Impaired Cerebrovascular Reactivity With Steal Phenomenon Is Associated With Increased Diffusion in White Matter of Patients With Moyamoya Disease. *Stroke* 41, 1610–1616.
- Conklin, J., Fierstra, J., Crawley, A.P., Han, J.S., Poubanc, J., Silver, F.L., Tymianski, M., Fisher, J.A., Mandell, D.M., Mikulis, D.J., 2011. Mapping white matter diffusion and cerebrovascular reactivity in carotid occlusive disease. *Neurology* 77, 431–438. <https://doi.org/10.1212/WNL.0b013e318227b1e7>
- De Vis, J.B., Petersen, E.T., Bhogal, A., Hartkamp, N.S., Klijn, C.J., Kappelle, L., Hendrikse, J., 2015. Calibrated MRI to Evaluate Cerebral Hemodynamics in Patients with an Internal Carotid Artery Occlusion. *J. Cereb. Blood Flow Metab.* 35, 1015–1023. <https://doi.org/10.1038/jcbfm.2015.14>
- Donahue, M.J., Ayad, M., Moore, R., van Osch, M., Singer, R., Clemmons, P., Strother, M., 2013. Relationships between hypercarbic reactivity, cerebral blood flow, and arterial circulation times in patients with moyamoya disease. *J. Magn. Reson. Imaging* 38, 1129–1139. <https://doi.org/10.1002/jmri.24070>
- Donahue, M.J., Strother, M.K., Lindsey, K.P., Hocke, L.M., Tong, Y., Frederick, B. deB., 2016. Time delay processing of hypercapnic fMRI allows quantitative parameterization of cerebrovascular reactivity and blood flow delays. *J. Cereb. Blood Flow Metab.* 36, 1767–1779. <https://doi.org/10.1177/0271678X15608643>
- Dubreuil, V., Ramanantsoa, N., Trochet, D., Vaubourg, V., Amiel, J., Gallego, J., Brunet, J.-F., Goridis, C., 2008. A human mutation in Phox2b causes lack of CO₂ chemosensitivity, fatal central apnea, and specific loss of parafacial neurons. *Proc. Natl. Acad. Sci.* 105, 1067–1072. <https://doi.org/10.1073/pnas.0709115105>
- Duffin, J., 2011. Measuring the respiratory chemoreflexes in humans. *Respir. Physiol. Neurobiol.* 177, 71–79. <https://doi.org/10.1016/j.resp.2011.04.009>
- Duffin, J., Sobczyk, O., Crawley, A.P., Poubanc, J., Mikulis, D.J., Fisher, J.A., 2015. The dynamics of cerebrovascular reactivity shown with transfer function analysis. *Neuroimage* 114, 207–216. <https://doi.org/10.1016/j.neuroimage.2015.04.029>
- Evans, K.C., Banzett, R.B., Adams, L., McKay, L., Frackowiak, R.S.J., Corfield, D.R., 2002. BOLD fMRI identifies limbic, paralimbic, and cerebellar activation during air hunger. *J. Neurophysiol.* 88, 1500–11.
- Ezra, M., Faull, O.K., Jbabdi, S., Pattinson, K.T., 2015. Connectivity-based segmentation of the periaqueductal gray matter in human with brainstem optimized diffusion MRI. *Hum. Brain Mapp.* 36, 3459–71. <https://doi.org/10.1002/hbm.22855>
- Faull, O.K., Jenkinson, M., Clare, S., Pattinson, K.T.S., 2015. Functional subdivision of the human periaqueductal grey in respiratory control using 7tesla fMRI. *Neuroimage* 113, 356–364. <https://doi.org/10.1016/j.neuroimage.2015.02.026>
- Faull, O.K., Pattinson, K.T., 2017. The cortical connectivity of the periaqueductal gray and the conditioned response to the threat of breathlessness. *Elife* 6, 1–18. <https://doi.org/10.7554/eLife.21749>
- Fierstra, J., Sobczyk, O., Battisti-Charbonney, A., Mandell, D.M., Poubanc, J., Crawley, A.P., Mikulis, D.J., Duffin, J., Fisher, J.A., 2013. Measuring cerebrovascular reactivity: what stimulus to use? *J. Physiol.* 591, 5809–21. <https://doi.org/10.1113/jphysiol.2013.259150>
- Friston, K.J., Josephs, O., Rees, G., Turner, R., 1998. Nonlinear event-related responses in fMRI. *Magn. Reson. Med.* 39, 41–52. <https://doi.org/10.1002/mrm.1910390109>
- Friston, K.J., Mechelli, A., Turner, R., Price, C.J., 2000. Nonlinear responses in fMRI: the Balloon model, Volterra kernels, and other hemodynamics. *Neuroimage* 12, 466–477. <https://doi.org/10.1006/nimg.2000.0630>
- Gaig, C., Irazzo, A., 2012. Sleep-Disordered Breathing in Neurodegenerative Diseases. *Curr. Neurol. Neurosci. Rep.*

- 12, 205–217. <https://doi.org/10.1007/s11910-011-0248-1>
- Golestani, A.M., Chang, C., Kwinta, J.B., Khatamian, Y.B., Jean Chen, J., 2015. Mapping the end-tidal CO₂ response function in the resting-state BOLD fMRI signal: Spatial specificity, test-retest reliability and effect of fMRI sampling rate. *Neuroimage* 104, 266–277. <https://doi.org/10.1016/j.neuroimage.2014.10.031>
- Gur, a Y., Bova, I., Bornstein, N.M., 1996. Is Impaired Cerebral Vasomotor Reactivity a Predictive Factor of Stroke in Asymptomatic Patients? *Stroke* 27, 2188–2190.
- Guyenet, P.G., Stornetta, R.L., Bayliss, D.A., 2010. Central respiratory chemoreception. *J. Comp. Neurol.* 518, 3883–3906. <https://doi.org/10.1002/cne.22435>
- Halani, S., Kwinta, J.B., Golestani, A.M., Khatamian, Y.B., Chen, J.J., 2015. Comparing cerebrovascular reactivity measured using BOLD and cerebral blood flow MRI: The effect of basal vascular tension on vasodilatory and vasoconstrictive reactivity. *Neuroimage* 110, 110–123. <https://doi.org/10.1016/j.neuroimage.2015.01.050>
- Hoskins, P.R., 1990. Measurement of arterial blood flow by Doppler ultrasound. *Clin. Phys. Physiol. Meas.* 11, 1–26.
- Hosseini-Zadeh, G.-A., Ardekani, B.A., Soltanian-Zadeh, H., 2003. A signal subspace approach for modeling the hemodynamic response function in fMRI. *Magn. Reson. Imaging* 21, 835–843.
- Iadecola, C., Nedergaard, M., 2007. Glial regulation of the cerebral microvasculature. *Nat. Neurosci.* 10, 1369–1376. <https://doi.org/10.1038/nn2003>
- Ide, K., Eliasziw, M., Poulin, M.J., 2003. Relationship between middle cerebral artery blood velocity and end-tidal PCO₂ in the hypocapnic-hypercapnic range in humans. *J. Appl. Physiol.* 95, 129–137. <https://doi.org/10.1152/japplphysiol.01186.2002>
- Jenkinson, M., Beckmann, C.F., Behrens, T.E.J., Woolrich, M.W., Smith, S.M., 2012. *Fsl*. *Neuroimage* 62, 782–790. <https://doi.org/10.1016/j.neuroimage.2011.09.015>
- Kaufman, L., Kaufman, L., Rousseeuw, P.J., Rousseeuw, P.J., 2005. *Finding Groups in Data: An Introduction to Cluster Analysis* (Wiley Series in Probability and Statistics), eepe.ethz.ch.
- Kaw, R., Hernandez, A. V., Walker, E., Aboussouan, L., Mokhlesi, B., 2009. Determinants of Hypercapnia in Obese Patients With Obstructive Sleep Apnea. *Chest* 136, 787–796. <https://doi.org/10.1378/chest.09-0615>
- Knuth, K.H., Ardekani, B.A., Helpert, J.A., 2001. Bayesian estimation of a parameterized hemodynamic response function in an event-related fMRI experiment, in: *Proc. of ISMRM*. p. 1732.
- Kontos, H.A., Raper, A.J., Patterson, J.L., 1977a. Analysis of vasoactivity of local pH, PCO₂ and bicarbonate on pial vessels. *Stroke* 8, 358–360. <https://doi.org/10.1161/01.STR.8.3.358>
- Kontos, H.A., Wei, E.P., Raper, A.J., Patterson, J.L., 1977b. Local mechanism of CO₂ action of cat pial arterioles. *Stroke* 8, 226–229. <https://doi.org/10.1161/01.STR.8.2.226>
- Lassen, N.A., 1968. Brain extracellular pH: the main factor controlling cerebral blood flow. *Scand. J. Clin. Lab. Invest.* 22, 247–51. <https://doi.org/10.3109/00365516809167060>
- Lucas, S.J.E., Tzeng, Y.C., Galvin, S.D., Thomas, K.N., Ogoh, S., Ainslie, P.N., 2010. Influence of Changes in Blood Pressure on Cerebral Perfusion and Oxygenation. *Hypertension* 55, 698–705. <https://doi.org/10.1161/HYPERTENSIONAHA.109.146290>
- Mandell, D.M., Han, J.S., Poubanc, J., Crawley, A.P., Kassner, A., Fisher, J.A., Mikulis, D.J., 2008a. Selective reduction of blood flow to white matter during hypercapnia corresponds with leukoaraiosis. *Stroke* 39, 1993–1998. <https://doi.org/10.1161/STROKEAHA.107.501692>
- Mandell, D.M., Han, J.S., Poubanc, J., Crawley, A.P., Stainsby, J.A., Fisher, J.A., Mikulis, D.J., 2008b. Mapping Cerebrovascular Reactivity Using Blood Oxygen Level-Dependent MRI in Patients With Arterial Steno-occlusive Disease: Comparison With Arterial Spin Labeling MRI. *Stroke* 39, 2021–2028.
- Mark, C.I., Fisher, J.A., Pike, G.B., 2011. Improved fMRI calibration: Precisely controlled hyperoxic versus hypercapnic stimuli. *Neuroimage* 54, 1102–1111. <https://doi.org/10.1016/j.neuroimage.2010.08.070>
- Markus, H., 2001. Severely impaired cerebrovascular reactivity predicts stroke and TIA risk in patients with carotid artery stenosis and occlusion. *Brain* 124, 457–467. <https://doi.org/10.1093/brain/124.3.457>
- Marmarelis, V.Z., 2004. *Nonlinear dynamic modeling of physiological systems*, Wiley. John Wiley & Sons. <https://doi.org/10.1002/9780471679370>
- Marmarelis, V.Z., 1993. Identification of nonlinear biological systems using Laguerre expansions of kernels. *Ann. Biomed. Eng.* 21, 573–89.
- Marmarelis, V.Z., Shin, D.C., Orme, M.E., Zhang, R., 2013. Model-based quantification of cerebral hemodynamics

- as a physiomarker for Alzheimer's disease? *Ann. Biomed. Eng.* 41, 2296–2317. <https://doi.org/10.1007/s10439-013-0837-z>
- Marmarelis, V.Z., Shin, D.C., Tarumi, T., Zhang, R., 2016. Comparison of Model-Based Indices of Cerebral Autoregulation and Vasomotor Reactivity Using Transcranial Doppler versus Near-Infrared Spectroscopy in Patients with Amnesic Mild Cognitive Impairment. *J Alzheimers Dis* 56, 89–105.
- McKay, L.C., Evans, K.C., Frackowiak, R.S.J., Corfield, D.R., 2003. Neural correlates of voluntary breathing in humans. *J. Appl. Physiol.* 95, 1170–1178. <https://doi.org/10.1152/japplphysiol.00641.2002>
- Mikulis, D.J., Krolczyk, G., Desal, H., Logan, W., DeVeber, G., Dirks, P., Tymianski, M., Crawley, A., Vesely, A., Kassner, A., Preiss, D., Somogyi, R., Fisher, J. a, 2005. Preoperative and postoperative mapping of cerebrovascular reactivity in moyamoya disease by using blood oxygen level—dependent magnetic resonance imaging. *J. Neurosurg.* 103, 347–355. <https://doi.org/10.3171/jns.2005.103.2.0347>
- Mitsis, G.D., Poulin, M.J., Robbins, P.A., Marmarelis, V.Z., 2004. Nonlinear modeling of the dynamic effects of arterial pressure and CO₂ variations on cerebral blood flow in healthy humans. *IEEE Trans. Biomed. Eng.* 51, 1932–43. <https://doi.org/10.1109/TBME.2004.834272>
- Mitsis, G.D., Zhang, R., Levine, B.D., Marmarelis, V.Z., 2002. Modeling of Nonlinear Physiological Systems with Fast and Slow Dynamics. II. Application to Cerebral Autoregulation. *Ann. Biomed. Eng.* 30, 555–565. <https://doi.org/10.1114/1.1477448>
- Mokhlesi, B., Tulaimat, A., 2007. Recent Advances in Obesity Hypoventilation Syndrome. *Chest* 132, 1322–1336. <https://doi.org/10.1378/chest.07-0027>
- Murphy, K., Harris, A.D., Wise, R.G., 2011. Robustly measuring vascular reactivity differences with breath-hold: Normalising stimulus-evoked and resting state BOLD fMRI data. *Neuroimage* 54, 369–379. <https://doi.org/10.1016/j.neuroimage.2010.07.059>
- Naganawa, S., Norris, D.G., Zysset, S., Mildner, T., 2002. Regional differences of fMR signal changes induced by hyperventilation: Comparison between SE-EPI and GE-EPI at 3-T. *J. Magn. Reson. Imaging* 15, 23–30. <https://doi.org/10.1002/jmri.10028>
- Orban, P., Doyon, J., Petrides, M., Mennes, M., Hoge, R., Bellec, P., 2014. The Richness of Task-Evoked Hemodynamic Responses Defines a Pseudohierarchy of Functionally Meaningful Brain Networks. *Cereb. Cortex* 25, 2658–2669. <https://doi.org/10.1093/cercor/bhu064>
- Panerai, R.B., 1998. Assessment of cerebral pressure autoregulation in humans—a review of measurement methods. *Physiol. Meas.* 19, 305–338. <https://doi.org/10.1088/0967-3334/19/3/001>
- Panerai, R.B., Simpson, D.M., Deverson, S.T., Mahony, P., Hayes, P., Evans, D.H., 2000. Multivariate dynamic analysis of cerebral blood flow regulation in humans. *IEEE Trans. Biomed. Eng.* 47, 419–423. <https://doi.org/10.1109/10.827312>
- Pattinson, K.T.S., Governo, R.J., MacIntosh, B.J., Russell, E.C., Corfield, D.R., Tracey, I., Wise, R.G., 2009. Opioids Depress Cortical Centers Responsible for the Volitional Control of Respiration. *J. Neurosci.* 29, 8177–8186. <https://doi.org/10.1523/JNEUROSCI.1375-09.2009>
- Pattinson, K.T.S., Mitsis, G.D., Harvey, A.K., Jbabdi, S., Dirckx, S., Mayhew, S.D., Rogers, R., Tracey, I., Wise, R.G., 2009. Determination of the human brainstem respiratory control network and its cortical connections in vivo using functional and structural imaging. *Neuroimage* 44. <https://doi.org/10.1016/j.neuroimage.2008.09.007>
- Pedersen, M.E.F., Fatemian, M., Robbins, P.A., 1999. Identification of fast and slow ventilatory responses to carbon dioxide under hypoxic and hyperoxic conditions in humans. *J. Physiol.* 521, 273–287. <https://doi.org/10.1111/j.1469-7793.1999.00273.x>
- Poublanc, J., Crawley, A.P., Sobczyk, O., Montandon, G., Sam, K., Mandell, D.M., Dufort, P., Venkatraghavan, L., Duffin, J., Mikulis, D.J., Fisher, J. a, others, 2015. Measuring cerebrovascular reactivity: the dynamic response to a step hypercapnic stimulus. *J. Cereb. Blood Flow Metab.* 1–11. <https://doi.org/10.1038/jcbfm.2015.114>
- Poulin, M.J., Liang, P.J., Robbins, P.A., 1996. Dynamics of the cerebral blood flow response to step changes in end-tidal PCO₂ and PO₂ in humans. *J. Appl. Physiol.* 81, 1084–1095.
- Prokopiou, P.C., Murphy, K., Wise, R.G., Mitsis, G.D., 2016. Estimation of voxel-wise dynamic cerebrovascular reactivity curves from resting-state fMRI data, in: 2016 IEEE 38th Annual International Conference of the Engineering in Medicine and Biology Society (EMBC). pp. 1143–1146. <https://doi.org/10.1109/EMBC.2016.7590906>
- Ramsay, S.C., Murphy, K., Shea, S.A., Friston, K.J., Lammertsma, A.A., Clark, J.C., Adams, L., Guz, A., Frackowiak,

- R.S., 1993. Changes in global cerebral blood flow in humans: effect on regional cerebral blood flow during a neural activation task. *J Physiol* 471, 521–534.
- Ratnatunga, C., Adiseshiah, M., 1990. Increase in middle cerebral artery velocity on breath holding: A simplified test of cerebral perfusion reserve. *Eur. J. Vasc. Surg.* 4, 519–523.
- Robbins, P.A., Conway, J., Cunningham, D.A., Khamnei, S., Paterson, D.J., 1990. A comparison of indirect methods for continuous estimation of arterial PCO₂ in men. *J. Appl. Physiol.* 68, 1727–31.
- Robbins, P.A., Swanson, G.D., Howson, M.G., 1982. A prediction-correction scheme for forcing alveolar gases along certain time courses. *J. Appl. Physiol.* 52, 1353–1357.
- Rostrup, E., Law, I., Blinkenberg, M., Larsson, H.B., Born, A.P., Holm, S., Paulson, O.B., 2000. Regional differences in the CBF and BOLD responses to hypercapnia: a combined PET and fMRI study. *Neuroimage* 11, 87–97. <https://doi.org/10.1006/nimg.1999.0526>
- Rousseeuw, P.J., 1987. Silhouettes: A graphical aid to the interpretation and validation of cluster analysis. *J. Comput. Appl. Math.* 20, 53–65.
- Shea, B.Y.S.A., Andres, L.P., Shannon, D.C., Banzett, R.B., 1993. Ventilatory Responses To Exercise in Humans Lacking 623–640.
- Silvestrini, M., Vernieri, F., Pasqualetti, P., Matteis, M., Passarelli, F., Troisi, E., Caltagirone, C., 2000. Impaired cerebral vasoreactivity and risk of stroke in patients with asymptomatic carotid artery stenosis. *JAMA* 283, 2122–7. <https://doi.org/10.1001/jama.283.16.2122>.
- Silvestrini, M., Viticchi, G., Falsetti, L., Balucani, C., Vernieri, F., Cerqua, R., Luzzi, S., Bartolini, M., Provinciali, L., 2011. The Role of Carotid Atherosclerosis in Alzheimer's Disease Progression. *J. Alzheimer's Dis.* 25, 719–726. <https://doi.org/10.3233/JAD-2011-101968>
- Slessarev, M., Han, J., Mardimae, A., Prisman, E., Preiss, D., Volgyesi, G., Ansel, C., Duffin, J., Fisher, J. a, 2007. Prospective targeting and control of end-tidal CO₂ and O₂ concentrations. *J. Physiol.* 581, 1207–19. <https://doi.org/10.1113/jphysiol.2007.129395>
- Smith, S.M., Nichols, T.E., 2009. Threshold-free cluster enhancement: addressing problems of smoothing, threshold dependence and localisation in cluster inference. *Neuroimage* 44, 83–98.
- Tancredi, F.B., Hoge, R.D., 2013. Comparison of cerebral vascular reactivity measures obtained using breath-holding and CO₂ inhalation. *J. Cereb. Blood Flow Metab.* 33, 1066–74. <https://doi.org/10.1038/jcbfm.2013.48>
- Thomas, B.P., Liu, P., Aslan, S., King, K.S., van Osch, M.J.P., Lu, H., 2013. Physiologic underpinnings of negative BOLD cerebrovascular reactivity in brain ventricles. *Neuroimage* 83, 505–512. <https://doi.org/10.1016/j.neuroimage.2013.07.005>
- Thomas, B.P., Liu, P., Park, D.C., van Osch, M.J.P., Lu, H., 2014. Cerebrovascular reactivity in the brain white matter: magnitude, temporal characteristics, and age effects. *J. Cereb. Blood Flow Metab.* 34, 242–7. <https://doi.org/10.1038/jcbfm.2013.194>
- Tzeng, Y.-C., Ainslie, P.N., 2014. Blood pressure regulation IX: cerebral autoregulation under blood pressure challenges. *Eur. J. Appl. Physiol.* 114, 545–559. <https://doi.org/10.1007/s00421-013-2667-y>
- Tzeng, Y.C., Macrae, B.A., Ainslie, P.N., Chan, G.S., 2014. Fundamental relationships between blood pressure and cerebral blood flow in humans. *J Appl Physiol.*
- Vinet, L., Zhedanov, A., 2010. A “missing” family of classical orthogonal polynomials. *Elife* 5, 1–19. <https://doi.org/10.1088/1751-8113/44/8/085201>
- von Leupoldt, A., Sommer, T., Kegat, S., Baumann, H.J., Klose, H., Dahme, B., Büchel, C., 2008. The Unpleasantness of Perceived Dyspnea Is Processed in the Anterior Insula and Amygdala. *Am. J. Respir. Crit. Care Med.* 177, 1026–1032. <https://doi.org/10.1164/rccm.200712-1821OC>
- Wang, D., Grunstein, R.R., Teichtahl, H., 2007. Association between ventilatory response to hypercapnia and obstructive sleep apnea-hypopnea index in asymptomatic subjects. *Sleep Breath.* 11, 103–108. <https://doi.org/10.1007/s11325-006-0090-x>
- Winkler, A.M., Ridgway, G.R., Webster, M.A., Smith, S.M., Nichols, T.E., 2014. Permutation inference for the general linear model. *Neuroimage* 92, 381–97. <https://doi.org/10.1016/j.neuroimage.2014.01.060>
- Wise, R.G., Ide, K., Poulin, M.J., Tracey, I., 2004. Resting fluctuations in arterial carbon dioxide induce significant low frequency variations in BOLD signal. *Neuroimage* 21, 1652–1664. <https://doi.org/10.1016/j.neuroimage.2003.11.025>

- Wise, R.G., Pattinson, K.T.S., Bulte, D.P., Chiarelli, P.A., Mayhew, S.D., Balanos, G.M., O'Connor, D.F., Pragnell, T.R., Robbins, P.A., Tracey, I., Jezzard, P., 2007. Dynamic forcing of end-tidal carbon dioxide and oxygen applied to functional magnetic resonance imaging. *J. Cereb. Blood Flow Metab.* 27, 1521–1532.
- Yezhuvath, U.S., Lewis-Amezcu, K., Varghese, R., Xiao, G., Lu, H., 2009. On the assessment of cerebrovascular reactivity using hypercapnia BOLD MRI. *NMR Biomed.* 22, 779–786. <https://doi.org/10.1002/nbm.1392>
- Yoon, S., Zuccarello, M., Rapoport, R.M., 2012. pCO₂ and pH regulation of cerebral blood flow. *Front. Physiol.* 3, 1–8. <https://doi.org/10.3389/fphys.2012.00365>

10. Supplementary Material

[Click here to download 10. Supplementary Material: Responses_to_reviewers_round_3_v3_supplementary.docx](#)